Graduate School ETD Form 9
(Revised 12/07)

PURDUE UNIVERSITY
GRADUATE SCHOOL
Thesis/Dissertation Acceptance

This is to certify that the thesis/dissertation prepared

By Parvin Ghane

Entitled
FABRICATION AND ANALYSIS OF CIGS NANOPARTICLE-BASED THIN FILM SOLAR CELLS

For the degree of Master of Science in Electrical and Computer Engineering

Is approved by the final examining committee:

Kody Varahramyan — Chair

Mangilal Agarwal

Maher Rizkalla

To the best of my knowledge and as understood by the student in the *Research Integrity and Copyright Disclaimer (Graduate School Form 20)*, this thesis/dissertation adheres to the provisions of Purdue University's "Policy on Integrity in Research" and the use of copyrighted material.

Approved by Major Professor(s): Kody Varahramyan

Approved by: Brian King — Head of the Graduate Program — 10/03/2012 — Date

Graduate School Form 20
(Revised 9/10)

PURDUE UNIVERSITY
GRADUATE SCHOOL

Research Integrity and Copyright Disclaimer

Title of Thesis/Dissertation:

FABRICATION AND ANALYSIS OF CIGS NANOPARTICLE-BASED THIN FILM SOLAR CELLS

For the degree of Master of Science in Electrical and Computer Engineering

I certify that in the preparation of this thesis, I have observed the provisions of *Purdue University Executive Memorandum No. C-22,* September 6, 1991, *Policy on Integrity in Research.**

Further, I certify that this work is free of plagiarism and all materials appearing in this thesis/dissertation have been properly quoted and attributed.

I certify that all copyrighted material incorporated into this thesis/dissertation is in compliance with the United States' copyright law and that I have received written permission from the copyright owners for my use of their work, which is beyond the scope of the law. I agree to indemnify and save harmless Purdue University from any and all claims that may be asserted or that may arise from any copyright violation.

PARVIN GHANE

Printed Name and Signature of Candidate

10/09/2012

Date (month/day/year)

*Located at http://www.purdue.edu/policies/pages/teach_res_outreach/c_22.html

FABRICATION AND ANALYSIS OF CIGS NANOPARTICLE-BASED THIN FILM SOLAR CELLS

A Thesis

Submitted to the Faculty

of

Purdue University

by

Parvin Ghane

In Partial Fulfillment of the

Requirements for the Degree

of

Master of Science in Electrical and Computer Engineering

December 2012

Purdue University

Indianapolis, Indiana

To those who have given me lives.

ACKNOWLEDGMENTS

I would like to thank all the people who supported and helped me through this research and thesis preparation. Special thanks to my adviser Prof. Kody Varahramyan, whose guidance was always brightening my pathway during my graduate education. Dr. Mangilal Agarwal and Dr. Sudhir Shrestha, whose consistent support and dedication to this research helped the progress and success of this work, need to be thanked the most. I would also like to thank these professors and Prof. Maher Rizkalla for their academic advising during my graduate study. I am very grateful for being associated with the Integrated Nanosystems Development Institute (INDI) at Indiana University-Purdue University Indianapolis (IUPUI) during this project and appreciate the facilities and support provided by the institute. Special thanks to research group members: Azadeh Hemati, Cansu Sener, Robert Vittoe, Ali Daneshkhah, Nojan Aliahmad, Jason Cambrige, Mark Canner, and Hossein Jafarian who made a warm working environment for me. I would like to express my gratitude to the faculty and staff members of the ECE department and School of Engineering and Technology at IUPUI, particularly Dr. Brian King and Mrs. Sherrie Tucker, for all their advice and assistance. I run out of words when it comes to my family, who has always been most supportive of me. I am pleased to have grown up in such a family and can never express my appreciation for all they have done for me.

TABLE OF CONTENTS

Page

LIST OF TABLES

LIST OF FIGURES

Figure Page

Appendix Figure

ABSTRACT

Ghane, Parvin. M.S.E.C.E., Purdue University, December 2012. Fabrication and Analysis of CIGS Nanoparticle-based Thin Film Solar Cells. Major Professor: Kody Varahramyan.

Fabrication and analysis of Copper Indium Gallium di-Selenide (CIGS) nanoparticles-based thin film solar cells are presented and discussed. This work explores non-traditional fabrication processes, such as spray-coating for the low-cost and highly-scalable production of CIGS-based solar cells.

CIGS nanoparticles were synthesized and analyzed, thin CIGS films were spray-deposited using nanoparticle inks, and resulting films were used in low-cost fabrication of a set of CIGS solar cell devices. This synthesis method utilizes a chemical colloidal process resulting in the formation of nanoparticles with tunable band gap and size. Based on theoretical and experimental studies, 100 nm nanoparticles with an associated band gap of 1.33 eV were selected to achieve the desired film characteristics and device performances. Scanning electron microcopy (SEM) and size measurement instruments (Zetasizer) were used to study the size and shape of the nanoparticles. Electron dispersive spectroscopy (EDS) results confirmed the presence of the four elements, Copper (Cu), Indium (In), Gallium (Ga), and Selenium (Se) in the synthesized nanoparticles, while X-ray diffraction (XRD) results confirmed the tetragonal chalcopyrite crystal structure. The ultraviolet-visible-near infra-red (UV-Vis-NIR) spectrophotometry results of the nanoparticles depicted light absorbance characteristics with good overlap against the solar irradiance spectrum.

The depositions of the nanoparticles were performed using spray-coating techniques. Nanoparticle ink dispersed in ethanol was sprayed using a simple airbrush tool. The thicknesses of the deposited films were controlled through variations in

the deposition steps, substrate to spray-nozzle distance, size of the nozzle, and air pressure. Surface features and topology of the spray-deposited films were analyzed using atomic force microscopy (AFM). The deposited films were observed to be relatively uniform with a minimum thickness of 400 nm. Post-annealing of the films at various temperatures was studied for the photoelectric performance of the deposited films. Current density and voltage (J/V) characteristics were measured under light illumination after annealing at different temperatures. It was observed that the highest photoelectric effect resulted in annealing temperatures of 150-250°C under air atmosphere.

The developed CIGS films were implemented in solar cell devices that included Cadmium Sulfide (CdS) and Zinc Oxide (ZnO) layers. The CdS film served as the n-type layer to form a pn junction with the p-type CIGS layer. In a typical device, a 300 nm CdS layer was deposited through chemical bath deposition on a 1 μm thick CIGS film. A thin layer of intrinsic ZnO was spray coated on the CdS film to prevent shorting with the top conductor layer, 1.5 μm spray-deposited aluminum doped ZnO layer. A set of fabricated devices were tested using a Keithley semiconductor characterization instrument and micromanipulator probe station. The highest measured device efficiency was 1.49%. The considered solar cell devices were simulated in ADEPT 2.0 solar cell simulator based on the given fabrication and experimental parameters. The simulation module developed was successfully calibrated with the experimental results. This module can be used for future development of the given work.

1. INTRODUCTION

1.1 Background on Renewable Energy and Photovoltaics

The current primary energy source in the US and most of other countries is fossil fuels. Although it seems the production of energy from fossil fuels costs the lowest among all other energy sources, its highly negative environmental and health effects have prompted the need to look for alternative sources.

Burning fossil fuels introduce a significant amount of carbon dioxide into the air. Increasing the percentage of carbon dioxide plays an important role in global warming. The warmer the earth gets, the faster glaciers melt, the higher the sea level rises, the more farm lands flood, and the more populated the lands get. Other than carbon dioxide, combustion of fossil fuels adds other toxic pollutants to the air. Breathing these pollutants can cause headaches, increase stress, and result in serious lungs diseases. Some of these pollutants combine with water in clouds and produce acid rain, which could make the environment too acidic for animals and plants and also damage buildings. Other than gaseous pollutants, the mining, production, and transportation of fossil fuels leave some waste productions in nature, which can adversely affect animals and plants.

Other than the biomedical and environmental effects of fossil fuels, energy consumption increases every year. As reported in International Energy Outlook 2011, the use of energy is expected to be increased by 53 percent from the year 2008 to 2035 (Figure 1.1) [1]. This happens while the price of oil, as one of the main supplies of fossil fuels, increases almost every year. According to OPEC basket price, the price of oil has shown an average increase of $8.34 per barrel per year in the last ten years [2]. Nuclear energy, as an alternative source of energy has significant safety and environmental concerns, including the proliferation of nuclear materials and disposal

of radioactive wastes. Furthermore, the disaster on March 2011 in Japan increased the worlds worry on the potentialy terrible effects of nuclear plant failure. As a result, Germany, Switzerland, and Italy announced a shut down of their reactors.

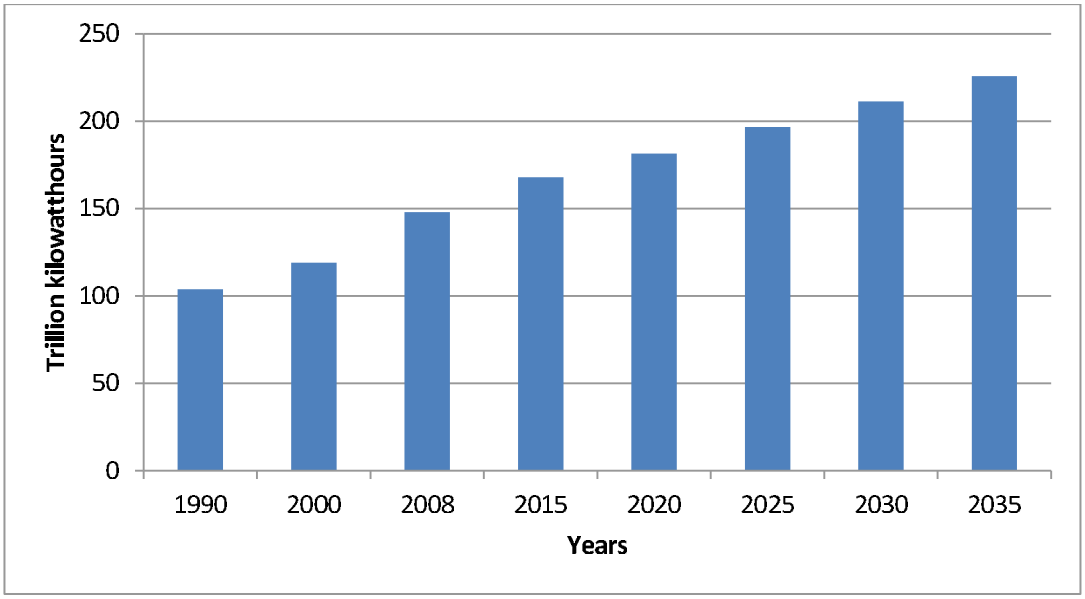

Fig. 1.1 Past and future projection of world energy consumption

The best alternative source of energy, one that could prevent all of these problems, is renewable energy. Other than preventing the mentioned problems, renewable energies support the security of energy supplies by providing private supplies. The generation of electricity is expected to increase by 84 percent from 2008 to 2035. Among the sources of electricity, renewable energies are expected to have the highest rate of growth (3.1 percent per year) [1]. Solar industry is one source of renewable energy that is developing rapidly. According to the SunShine Vision Study by Department of Energy, it is expected that solar energy satisfies 14% of the electricity need of U.S. by 2030 and 27% by 2050. This means the installation of about 302 GW of photovoltaic systems by 2030 and 632 GW by 2050. As a result, an 8% reduction in carbon dioxide emissions by 2030 and 28% reduction by 2050 are expected. These advantages will be achieved while only about 0.11%-0.33% U.S. land area would require the installation of solar equipment by 2050 [3].

In order to support such expectations about 75% reduction in production costs associated with solar technologies must be implemented by 2020. The goal is to reach "$1/W for photovoltaic systems (PV), $1.25/W for commercial rooftop PV, and $1.5/W for residential rooftop PV". The average retail price for households would be 0.9 cents/kilowatt-hour(kWh), saving $9 per month per household and $50 billion in annual savings by 2050. The employment of such a plan will provide 390,000 new jobs by 2050 [3].

Current Photovoltaic Technology Outlook

In alignment with the SunShot study, the price of manufacturing modules decreased from $60/W in 1976 to $2/W in 2010 [4]. PV installation in the US in 2011 had %109 growth over 2010 with 1,855 MW of photovoltaic systems [5]. The installation of PVs continued on 2012 with installing 506 MW of PVs on the first quarter of the year. Prediction of installation of 3.3 GW of PV solar systems in the US by the end of 2012, 11% of the global installation [6]. The growth in the consumption of PV systems has increased employment rates as well. The 37% increase in installations from 2008 to 2009 gave 17,000 new job opportunities, supporting 46,000 jobs related to solar industry in the U.S. [7]. On the other hand, although nuclear power is considered as one of the major sources of energy, on a trade off done by Blackburn and Cunningham, the costs of PV systems were comparable to the cost of nuclear power plans, while the former is steadily decreasing and the latter is increasing. The cost of solar energy generation is estimated to be less than 10 cents per kWh, while would be 25 cents for nuclear power [8].

1.2 Review of Thin-Film Solar Cell Materials and Fabrications

While it was reported that about 85% of the 2011 PV market belonged to crystalline silicone [4], it is expected that the production of thin film solar cells increases in 2012 and 2013 as many related facilities have invested on this technology and have

been starting their production line [5]. The thin film market has increased in production capacity of 46% for Cadmium Telluride (CdTe) and 13% for Compound of Copper Indium Gallium di-Selenide(or Sulphur) (CIGS) from 2010 to 2011 [5].

In general, a solar cell consists of a pair of p and n type semiconductors that absorb photons, creating of electron-hole carriers, and conducting of the carriers in electrical circuits. Types of solar cells are distinguished by the type of absorbers. While crystalline silicon solar cells use an absorber layer with a thickness in the range of a milimeter, thin film solar cells need only a few micron thick absorber. This characteristic of thin film solar cells makes them much lighter than conventional silicon solar cells and provides the possibility of manufacturing flexible solar cells. Crystalline silicon solar cells consists of wafers that tile together to form the module area, while thin film cells can be coated on a single large and continues substrate. Such a structure, along with lower material quantity results in lower cost per unit area. Other than manufacturing cost, the efficiency is another important parameter in determining the expenses of PV consumption. The efficiency of a PV is defined as the output power generated by the system in response to the input power it absorbs from photons. Figure 1.2 shows the best efficiency of cells manufactured in labs to date [9].

Currently, the largest share of thin film solar cells belongs to CdTe [5]. However, due to the dangerous health effects of CdTe, these panels have to be recycled properly. After CdTe, CIGS-based solar cells have the highest share in the thin film solar cell market. Also, as indicated in Figure 1.2, CIGS-based solar cells have the highest efficiency among the thin film solar cells due to the appropriate band gap of CIGS (tunable between 1.02 to 1.67). Furthermore, unlike many other thin film solar cells, CIGS-based PVs have good stability and do not show any major degradation under illumination, which provides a lifetime close to the conventional solar cells [10]. A high absorption coefficient and photon-to-current-conversion efficiency makes CIGS one of the best candidates for thin film solar cells. However, the fabrication of low

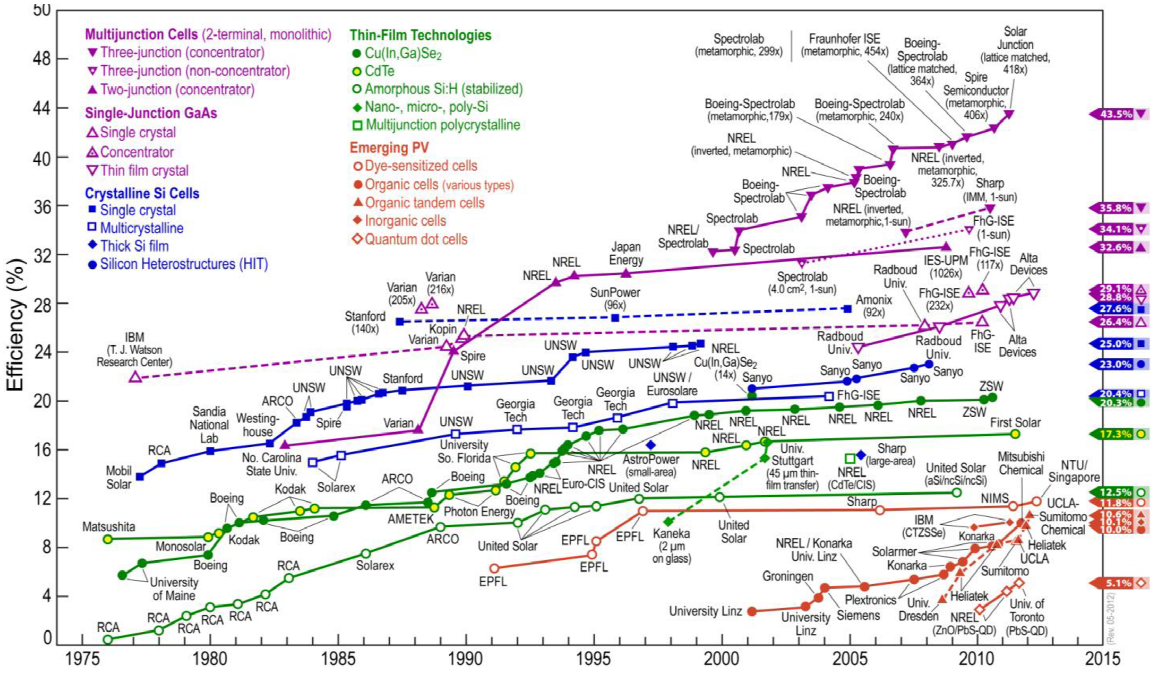

Fig. 1.2 Best laboratory cell efficiency from 1976 to date [9]

cost and high efficiency CIGS solar cells in large scale is still a barrier in the high production of such modules.

To date, the most efficient CIGS-based solar cells are reported to have 20.3% efficiency and have been fabricated via a three-stage co-evaporation process [11]. In this process, which was first reported by National Renewable Energy Laboratory (NREL), precursors of $(In,Ga)_xSe_y$ are co-evaporated on a substrate, followed by deposition of Cu and Se. Later, In, Ga, and Se are deposited to readjust the Cu concentration at the final stage. This method provides very smooth CIGS film surfaces, reducing the junction area and consequently lowering interface defect states [12]. This process gives the ability of depositing a graded absorber layer by variation of the In/Ga flux ratio. Graded absorbers help to find the optimum band gap for a trade-off between open circuit voltage and short circuit current. High open circuit voltage can be achieved by increasing the absorber's band gap, while higher band gap reduces photon absorption and electron-hole generation to lower short circuit current. Another vacuum-based

deposition process for production of CIGS solar cell is sputtering. In this process metallic alloysare sputtered on a substrate followed by metal selenide precursors [14] or a selenization step [13].

Even though vacuum-based processes result in smooth and highly efficient films, its high fabrication cost is a barrier to replace fossil fuels. Furthermore, the modules produced by this process are limited to the size of the vacuum chamber. Non-vacuum based fabrication techniques, also referred as low cost processes, are used to solve these issues. Dropcasting, spin coating, electrodeposition, inkjet printing, rolling printing, paste coating, and spraying pyrolysis and precursors are some non-vacuum techniques that have been investigated. The efforts reported in [15] and [16] are some examples of dropcasting experiments, which do not seem to be scalable. Liu et al. [17] reported spin coating technique by dissolving material in hydrazine, a toxic and explosive chemical that limits the industrial production scale. Harati et al. [18] demonstrated electrodeposition of materials, requiring the availability and control of soluble salts of all four elements. In spray coating of pyrolysis [19] and precursors [20] the four elements were sprayed for the formation of CIGS on the substrate, which increases the possibility of formation of byproducts, reduces the controllability on the stoichiometry of the final CIGS product and bandgap. Furthermore, the elemental solutions in the latter are dissolved in toxic hydrazine. Inkjet printing, rolling printing, and paste coating have also been studied in [21–23] to scale up the process but still have low efficiencies. In general, the fabrication of CIGS-based thin film solar cells to achieve low cost, high efficiency and scalable processes is still under investigation.

1.3 Contributions of this Thesis Research

In this project CIGS nanoparticles were synthesized and analysed, thin films of solar cell were deposited and functionalized, and the integration of films to solar cell was fabricated and tested. All processes reported in this project are low cost and highly scalable with a high potential for commercial production.

CIGS nanoparticles were synthesised via a high throughput chemical colloidal process. The size and band gap of nanoparticles synthesized through this process are highly controllable. Synthesis was performed under Nitrogen atmosphere, in Oleylamine environment. The particles were cleaned, purified, and their physical and chemical properties were tested. Physical analysis of the particles included size and shape (by SEM and nanosizer), light absorption (by UV-Vis-NIR spectroscopy), and band gap calculation. Chemical analysis consisted of the study of the constituent elements (by EDS) and crystallography (by XRD).

SEM images of provided the observation of size and shape of the nanoparticles, while the nanosizer results confirmed the size distribution statistically. Based on the target particle size, they were divided to classes with average diameters ranging from 100 to 400 nm $\pm$26 nm. UV-Vis-NIR spectroscopy of particles confirmed high absorption of photons with wavelength ranging from 300 to 1100 nm. Band gaps of the nanoparticles were calculated with the help of light absorption and Tauc's relationship. The band gap was approximately 1.35 ev, which could be modified by changing the ratio of the initial Copper, Indium, Gallium, and Selenium elements. EDS verified the existence of all four elements in single and clumps of particles, while XRD confirmed their tetragonal chalcopyrite crystalline structure.

Solutions of nanoparticles were prepared for deposition through spray coating, as a simple, low cost, and scalable process. The nanoparticles were dispersed in ethanol and well sonicated to produce a uniform film. The film was sprayed on substrate with the help of an airbrush. The deposited film was analysed in terms of roughness and thickness via AFM imaging. The roughness of the film was about 100 nm, which was in alignment with the average particle size. The film thickness was controllable ranging from 2 to thicker than 3 μm. The electrical characteristiztion of a film of CIGS showed a good response to light, confirming the ability of this layer to be used for solar cell application.

The CIGS film, as an absorber, in combination with a film of Cadmium Sulfide (CdS) and intrinsic Zinc Oxide (i-ZnO), as buffers, and Aluminium doped Zinc

Oxide(Al-ZnO), as a front contact, were used to represent a thin film CIGS solar cell. CdS was deposited via simple and scalable Chemical Bath Deposition, combining Cadmium Sulfate, Thiourea, Ammonium Hydroxide, and water. The thickness of this layer could be controlled by managing the initial materials and the deposition time. The thickness of this layer was analysed by AFM imaging. It was decided to use thickness of 300 nm for this layer. ZnO layers were spray deposited in a process similar to the deposition of CIGS. The thickness of ZnO layers were also analysed by AFM imaging. This layer was thicker than expected (1.5 μm), reducing the transparency and efficiency of the overall solar cell.

The fabricated solar cell was simulated by ADEPT 2.0 software, applying physical parameters and measurement conditions. The fabricated solar cell showed a good alignment with the simulation results, giving an open-circuit voltage of 0.2 V, short-circuit current density of about 3 $\mu A/cm^2$, and 1.5% efficiency.

2. THEORY

2.1 Physics of Solar Cell

Every solar cell consists of a photon-absorbing layer. When a photon with energy (E_{ph}) equal to the band gap of the absorber (E_g) hits an electron in the valance band of the absorber layer, it excites that electron, which leaves the valance band and jumps to the conduction band. If (E_{ph})>(E_g), the electron will use the energy to jump above the conduction band edge and then relax down to the conduction band edge by releasing the extra energy as heat(thermalisation). The process of exciting valance band electrons to the conduction band and leaving holes in the valance band is called electron-hole generation .

If the generated carriers are not separated appropriately, they will recombine without contributing in the current generation. One way to separate the carriers is applying an electric field. A p-n junction can produce such an electric field and is the connection of p and n-type semiconductors. A p-type semiconductor is a material with a high density of holes compared to electrons. Likewise, an n-type semiconductor has a higher electron density compared to holes. If both p and n sides consist of the same material, the pn junction is called a homojunction (e.g. Si solar cell); if they are made of different materials, the pn junction is called a heterojunciton (e.g. CIGS solar cell). When a pair of p and n-type semiconductors are brought together, the carriers move from the region with high density to the one with lower density. In other words, the electrons move from n-type to p-type and the holes will move in the opposite direction. Such movement of carriers is caused by the concentration gradient and is called diffusion.

Diffusion of carriers causes the vicinity of the junction to be depleted of carriers (depletion region), leaving ions behind. Positively charged ions in n side and nega-

tively charged ions in p side result in an electric field with direction opposite diffusion. The movement of free carriers in this electric field is called drift current. In equilibrium, drift and diffusion currents are equal, resulting in zero net current. In a solar cell, the generated carriers get separated by the p-n junction electric field.

CIGS Solar Cell

The p-n junction in CIGS solar cells is a heterojunction type. As it is explained in Section 2.3, in such solar cells CIGS acts as the p-type absorber. Attachment of CdS (an n-type material) and highly n-doped TCO constructs the pn junction that was explained earlier. The difference in electron affinity (χ) of p-type CIGS (4.1 ev) and n-type CdS (3.8 ev) causes a conduction band discontinuity (ΔE_c)(see Figure 2.1) . If ΔE_c is higher than 0.5 ev, it will generate a barrier as the generated electrons move to the n-type side. If ΔE_c is zero or negative, the valance band at the edge of the junction gets too close to the conduction band of n-doped side and recombination at the buffer/absorber interface increases [24, 25].

The maximum photovoltage that can be achieved from a CIGS solar cell is determined from band bending (V_{bb}). V_{bb} can be calculated form the difference between the maximum valance band outside of depletion region and Fermi level and from the the difference between Fermi level and absorber's valance band at the edge of the junction (ξ). Increasing the bandgap of the absorber will increase the band bending and therefore increases the obtainable photovoltage [26]. Increasing Ga content in CIGS increase its band gap and helps increase photovoltage generation. However, due to the decrease in photocurrent after a curtain band gap the photovoltage saturates and the efficiency of the device is reduced.

Another positive point of using CdS as the n-type buffer layer is the CIGS surface modification when it is contacted with CdS. During the formation of CIGS-CdS heterojunction, some Cu-vacancies are generated at the surface of CIGS. These vacancies reduce the valance band at the surface of CIGS, increasing ξ and band bending [26].

In general, ξ is determined by the doping levels of absorber and TCO and the thickness of buffer layers. Even though the main p-n junction happens between CIGS and CdS, the front contact TCO plays a main role in the position of the Fermi level. This is due to the higher thickness and doping of TCO compared to other buffer layers.

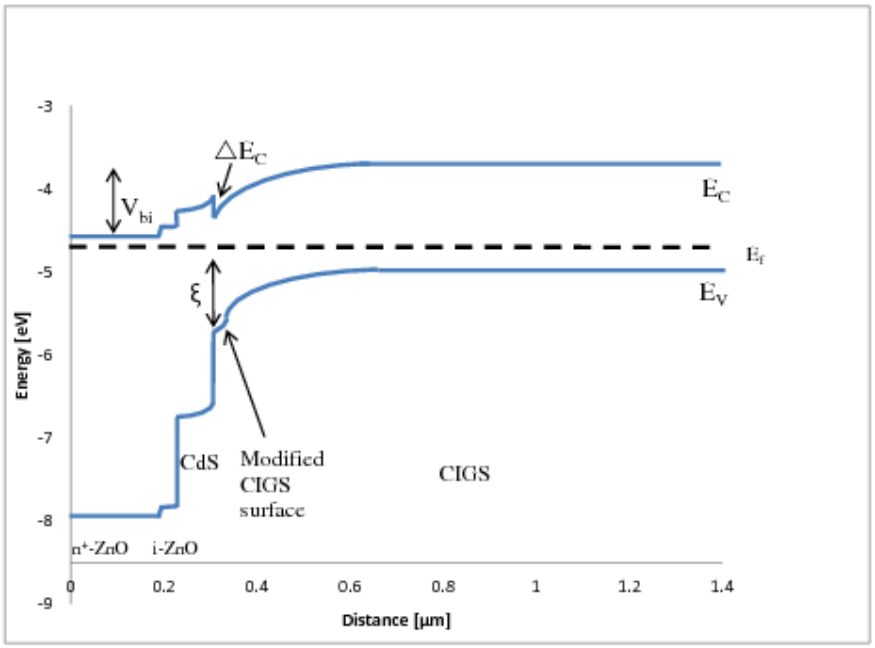

Fig. 2.1 Band Diagram of a CIGS Solar Cell

Quantum Efficiency

In a solar cell, the number of electron-hole pairs generated by the light incident and contributed in the conduction of current is considered as the response of the cell to wavelengths of that light source. This ability can be expressed by Quantum

Efficiency (QE). QE is the ratio of the number of carrier pairs contributed in the current generation of solar cell to the number of the photons at a specific wavelength incident the solar cell. As explained before, no photons with energies below the band gap can be absorbed. If all photons with a specific wavelengths are absorbed and the generated carriers contribute in the current generation, QE at that wavelength would be unity. However, in reality this is usually not the case due to the recombination of a portion of generated pairs.

$$QE = \frac{(number of electron - hole pairs collected by solar cell)/sec}{(number of photons with a given energy incident the solar cell)/sec} \tag{2.1}$$

2.2 Mathematical Models

2.2.1 Transport Equations

The behaviour of semiconductor materials and devices is described by a set of three equations: *Poisson*, and *Continuity* equations.

The Poisson equation is usually used to obtain quantitative solutions for the electric field in semiconductors. This equation relates the variation of electric field in a volume to the charge enclosed by that volume. Poisson's equation in three dimensional space is

$$\bigtriangledown . E = - \bigtriangledown^2 . \psi = - \frac{\rho}{K_S \varepsilon_0} \tag{2.2}$$

where ψ is electric potential, E is the electric field, ε_0 is the permittivity of free space, K_S is the semiconductor's dielectric constant, and ρ is local charge density (charge/cm^3). In the one dimentional case, where $E = E_x$, Poisson equation becomes

$$\frac{d^2 \psi}{dx^2} = - \frac{dE}{dx} = - \frac{\rho}{K_S \varepsilon_0} \tag{2.3}$$

Charge density consists of the holes, negatively-charged ionized acceptors, electrons, and positively-charged ionized donors. Assuming the dopants are fully ionized, the charge density would be

$$\rho = q(p - n + N_D - N_A) \tag{2.4}$$

Continuity equations describe variation in the carrier concentration. If we consider a differential volume Adx, variation of number of free electrons in the volume can be found by the number of electrons entering the volume, minus the number of electrons leaving the volume, plus the number of electrons generated in the volume, minus the number of those recombined.

$$A\frac{\partial n}{\partial t}dx = A(\frac{J_n(x)}{-q} - \frac{J_n(x+dx)}{-q}) + A(G_n - U_n)dx \tag{2.5}$$

which leads to continuity equations for electrons in one dimensional case as

$$\frac{\partial n}{\partial t} = \frac{1}{q}(\frac{\partial J_n}{\partial x}) + (G_n - U_n) \tag{2.6}$$

Similar calculations give the continuity equations for holes in one dimensional case as

$$\frac{\partial p}{\partial t} = -\frac{1}{q}(\frac{\partial J_p}{\partial x}) + (G_p - U_p) \tag{2.7}$$

Expanding Equations 2.6 and 2.7 to three dimensions gives the continuity equations in 3D space for electrons 2.8 and holes 2.9.

$$\frac{\partial n}{\partial t} = \frac{1}{q}divJ_n + (G_n - U_n) \tag{2.8}$$

$$\frac{\partial p}{\partial t} = -\frac{1}{q}divJ_p + (G_p - U_p) \tag{2.9}$$

The variation of current densities ($divJ_p$ and $divJ_n$) in continuity equations are derived from drift and diffusion processes. Drift and Diffusion currents that were introduced above can be expressed with

$$J_p = q\mu_p pE - qD_p\nabla(p) \tag{2.10}$$

$$J_n = q\mu_n nE - qD_n\nabla(n) \tag{2.11}$$

where J_p and J_n are the overall drift-diffusion current density of holes and electrons, respectively. In these equations, the first part represents the drift current, while the second part shows the diffusion current flow. In these formulas, E is electric field and q is electron charge; μ_p and μ_n are mobilities; D_p and D_n are diffusion constants;

and p and n are the carrier density for holes and electrons, respectively. In the one dimensional case (x direction) Equations 2.10 and 2.11 simplify to

$$J_p = q\mu_p pE - qD_p\frac{dp}{dx} \tag{2.12}$$

$$J_n = q\mu_n nE - qD_n\frac{dn}{dx} \tag{2.13}$$

This set of five *Poisson*, *Continuity*, and *Drift-Diffusion* equations is called "Transport Equations" [27–29].

2.2.2 Electrical Characteristics

As explained in the previous sections, in general, a solar cell is made of a pn junction. Therefore, in dark, where there is no electron-hole generation, as the solar cell acts as a diode. The current of a diode could be calculated from

$$I_{dark} = I_{diode} = I_0(e^{\frac{qV}{nkT}} - 1) \tag{2.14}$$

where q is elementary charge, k is Boltzman's constant, and T is the absolute temperature in Kelvin. n is the ideality factor and simulates the deviation of a real diode from ideal diode. An ideality factor close to 1 indicates that major recombination happens in the bulk, while an ideality factor of 2 means most of the recombination takes place in the deplation region [30]. I_s is reverse saturation current and depends on device temperature and material properties can be found from

$$I_s = qA(\frac{D_N}{L_N}\frac{n_i^2}{N_D} + \frac{D_P}{L_P}\frac{n_i^2}{N_A}) = qA(\frac{L_N}{t_N}n_p + \frac{L_P}{t_P}p_n) \tag{2.15}$$

where A is the cross section of the p-n junction, n_i is the carrier density of the intrinsic material; L_N and L_P are the minority carrier diffusion length; D_N and D_P are the diffusion coefficients; t_N and t_P are the minority carrier lifetime; n_p and p_n are the number of minority carriers and N_A and N_D are the number of majority carriers of p and n side, respectively. The second part of Equation 2.15 has been derived from Equations 2.16 and 2.17 for either carrier type.

$$L = \sqrt{D.t} \tag{2.16}$$

$$\frac{D}{\mu} = \frac{kT}{q} \tag{2.17}$$

Equation 2.17 is well-known as the Einstein equation. It allows the calculation of either diffusion coefficient (D) or mobility (μ) from the other.

When solar cells are exposed to light, electron-holes will be generated, producing generation current (I_L) in direction opposite to I_{dark} (due to the generation and movement of minority carriers). This current can be found from

$$I_L = -qA(L_N + W + L_P)G \tag{2.18}$$

where G is the generation rate, W is the width of the pn junction and could be found from. W is determined by the carrier density of both n and p sides by

$$W = x_n + x_p = [\frac{2K_S\varepsilon_0}{q}(\frac{N_A + N_D}{N_A N_D})V_{bi}]^{1/2} \tag{2.19}$$

where x_n and x_p are the boarders of depletion region in n and p sides, respectively. The relationship between these two parameters in a pn junction is

$$N_A x_p = N_D x_n \tag{2.20}$$

V_{bi} is the built in potential of the pn junction with depletion region's lengths of x_n and x_p in n and p sides. Built in potential can be found from doping density of the two sides

$$V_{bi} = \frac{kT}{q} ln \frac{n(x_n)}{n(-x_p)} = \frac{kT}{q} ln \frac{N_A N_D}{n_i^2} \tag{2.21}$$

where the second equation was driven from

$$n(x_p) = \frac{n_i^2}{N_A} \tag{2.22}$$

The amount of light absorbed at any point of the material depends on the light intensity at the top surface (I_0), absorption coefficient (α in cm^{-1}) of material and the depth of that point inside the material(x). Neglecting the reflection, the absorption of light at point x from the surface of material would be

$$I = I_0 e^{-\alpha x} \tag{2.23}$$

If all of absorbed light results in the generation of electron-hole pair, the change in the light intensity across the material could determine the generation rate (G). Therefore, differentiating Equation 2.23 results in the generation rate at any point of material.

$$G = \alpha N_0 e^{-\alpha x} \tag{2.24}$$

where $N_0(\frac{\#photons}{(unit-area).(sec)})$ is the photon flux density, number of photons incident on unit area in unit time, at the surface of material. I_L can also be calculated for light incident with energy E by [31]

$$I_L(E) = qA \int N_0(E) QE(E,V) dE \tag{2.25}$$

assuming all carriers generated in the depletion region participate in the photogeneration current and do not recombine and the ones generated outside the depletion region diffuse to the edge of this region, quantum efficiency can be found by [32]

$$QE(E,V) \approx 1 - \frac{exp[-\alpha(E)W(V)]}{\alpha(E)L + 1} \tag{2.26}$$

The overall current of a solar cell would be the addition of these two currents. Therefore the IV characteristic for an ideal solar cell is calculated from:

$$I(V) = I_{diode}(V) + I_L = I_0(e^{(\frac{qV}{nkT})} - 1) + I_L \tag{2.27}$$

using Equations 2.14 and 2.18 the overall current would be

$$I(V) = I_0(e^{(\frac{qV}{nkT})} - 1) - qA(L_N + W + L_P)G \tag{2.28}$$

In an ideal case, when the series resistance is assumed to be zero, the IV of the device under light illumination would be the same as the one in dark, shifted down for I_L (Figure 2.2) [33]. There are four parameters that have to be studied in order to characterise the output of a solar cell. These are short circuit current (I_{sc}), open circuit voltage (V_{oc}), fill factor (FF), and energy conversion efficiency (η).

Open-circuit voltage could be found from the generated current and Equation 2.27 when there is no current flowing through the device.

$$V_{oc} = \frac{nkT}{q} ln(\frac{I_L}{I_0} + 1) \tag{2.29}$$

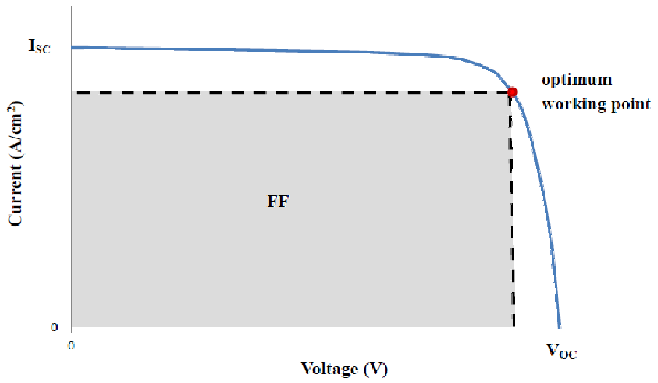

Fig. 2.2 Current voltage Characteristic of an Ideal Solar Cell

Fill factor is a measurement of how rectangular the IV curve is and is defined by

$$FF = \frac{V_{mp} I_{mp}}{V_{oc} I_{sc}} \tag{2.30}$$

V_{mp} and I_{mp} are the voltage and current of the point with the highest output power (P_{max}=I_{mp}.V_{mp}). The efficiency of a solar cell is defined as the maximum output power divided by the total power of the incident light on solar cell.

$$\eta = \frac{I_{mp} V_{mp}}{P_{in}} = \frac{I_{sc} V_{oc} FF}{P_{in}} \tag{2.31}$$

P_{in} is usually taken as 100 mW/cm^2 to simulate AM1.5 as standard solar illumination.

Circuit Model

Equation 2.27 considers an ideal solar cell. In practice, there are some lose in the generated current due to parasitic resistances. The power dissipation through the solar cell is shown via parasitic resistances.

Parasitic resistances are an illustration of power dissipation in the bulk material, on interconnections (series resistance R_s) and current leakages through the cell (shunt resistance R_{sh}). Series resistance represents any ohmic-wanted connections such as between the layers, between semiconductors and metallic contacts, in metallic contacts, and in the bulk materials (layers). All the high resistive paths in parallel with

the pn junction are shown by shunt resistance R_{sh}. These paths can be made due to the impurity, crystal damage, and induction of defects at the junction or any paths with resistance less than the desired current path around the edges [34]. Figure 2.3 a shows one diode circuit model (compared to the two diode circuit model [34]) for solar cells. In this model, a solar cell is shown by a current source which generates I_L and a diode biased in parallel and reverse direction. Based on this model Equation 2.27 should be modified to

$$I(V) = I_{diode}(V) - I_L + \frac{V - IR_s}{R_{sh}} \tag{2.32}$$

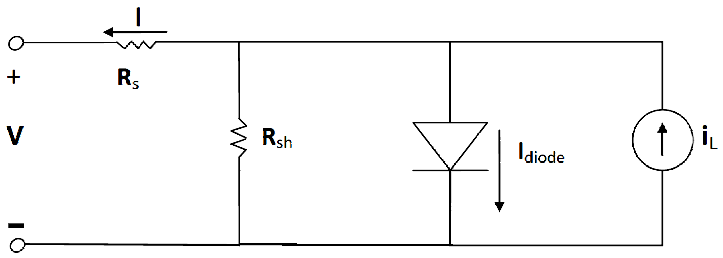

Fig. 2.3 Solar cell one diode equivalent circuit model

It is clear from Equation 2.32 and Figure 2.3 that in order to have the least power dissipation, R_S and R_{sh} should to be the lowest and highest, respectively.

2.3 CIGS Crystal Structure

Copper $\text{Indium}_{(1-x)}$ $\text{Gallium}_{(x)}$ Selenium_2 (CIGS) chalcopyrite is a I-III-IV semiconductor with a direct band gap and high absorption coefficient (10^5 cm^{-1}) [18]. The band gap of this compound changes from 1.02 to 1.67ev when x changes from zero to one by Equation 2.33, where the major change occurs in the conduction band [35,36].

$$E_g(ev) = 1.02 + 0.67x + 0.11x(x-1) \tag{2.33}$$

The band gap of 1.1 to 1.7 matches the solar spectrum quite well and makes CIGS a suitable material to be used in thin film solar cells. A 1 μm thick layer

of CIGS absorbs a sufficient amount of light photons and generates current. Using nanoparticles of CIGS chalcopyrite gives the ability to produce a thinner absorber layer and lighter devices. Furthermore, it reduces fabrication cost, as less material is used. The thickness limitations and synthesis of CIGS nanoparticles will be discussed later.

The zinc blende molecular structure of CIGS chalcopyrite is shown in Figure 2.4. In this lattice, each atom of Se at the center of tetrahedral unit cell connects to two atoms of Cu and In/Ga. Similarly, each atom of Cu, In, or Ga is surrounded by a tetrahedron of Se atoms.

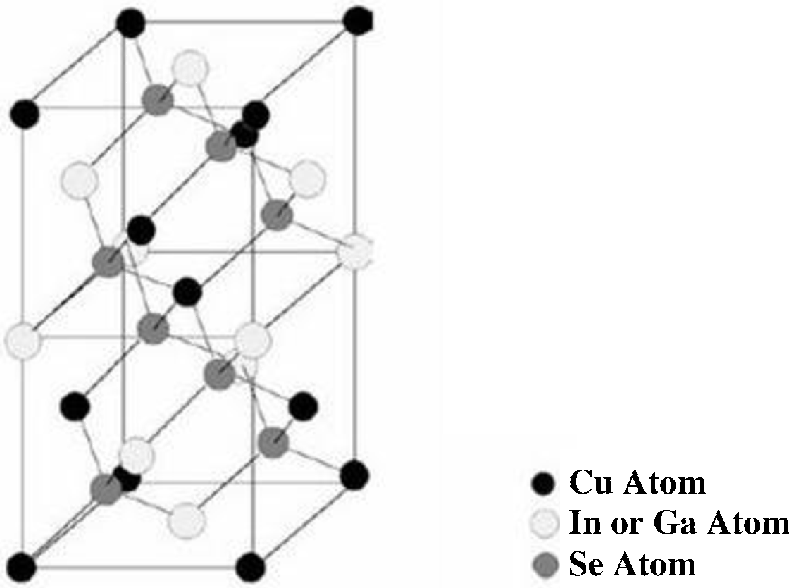

Fig. 2.4 Zinc blende structure of CIGS chalcopyrite crystal

CIGS is known as a p-type semiconductor, which is due to the defects produced by Copper vacancy in its structure. Copper rich CIGS causes the formation of $CuSe_2$, which is highly conductive and shorts the junction in solar cell. Oppositely, Se vacancy introduces defects that tend to make the material n-type. Therefore, if p-type CIGS is desired, Copper-poor samples will be made and annealed under Se atmosphere (Selenization) [37–39].

2.4 CIGS Solar Cell

The most efficient and common structure for CIGS based solar cells is shown in Figure 2.5. This structure is made of a substrate, Molybdenum (Back contact), CIGS (absorber layer), Cadmium Sulfide (window layer), intrinsic Zinc Oxide (buffer layer), and a transparent conductive layer such as aluminium doped Zinc Oxide for the front contact. The current will be collected by a metallic mesh, usually aluminium-nickel, spread on top of the front contact layer. This chapter will explain the role of each layer in the performance of the overall device.

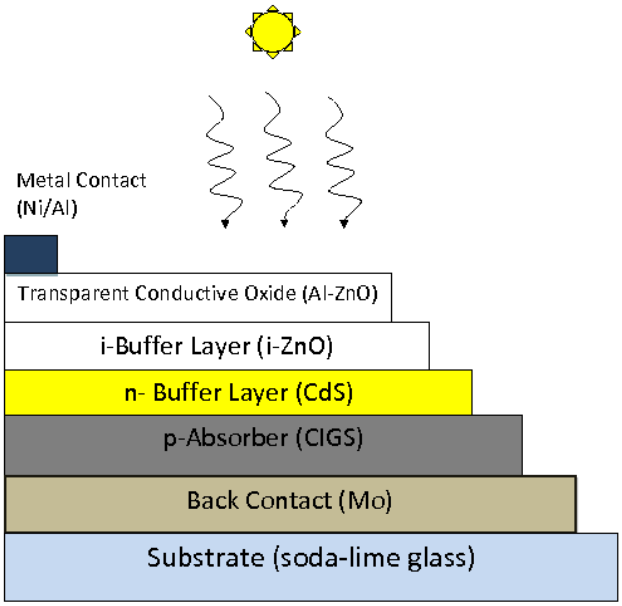

Fig. 2.5 Schematic depiction of Llayers in a CIGS solar cell

Substrate

All layers of a solar cell are deposited on a substrate. Therefore the substrate has to have appropriate properties to maintain unchanged during several deposition processes and provide a stable device. These properties include thermal expansion

properties and melting point, chemical composition, and stability under vacuum or low pressure and over time.

The most common substrate used for CIGS solar cell is soda lime glass (SLG). Rather than having the above properties it has been reported that the sodium content in SLG could diffuse into the CIGS layer and improve its grain growth and decrease its resistivity up to two times, resulting in increase cell performance [40, 41].

The use of flexible substrates has attracted a lot of attention during the past years. Solar cells on stainless steel, metal foils, conductive plastics and polymers have been reported with efficiencies of 12.3%, 17.6%, 15%, and over 15%, respectively [41–44].

Back Contact

Back contact is the first layer in connection with the CIGS absorber layer which contributes in the flow of current (Figure 2.5). Therefore it has to be conductive, make ohmic contact with CIGS, have a low minority carrier recombination rate, and remain stable during the fabrication process. Also, having a high light reflection can increase the generation rate of minority carriers in very thin solar cells. Having a very low minority carrier's recombination rate plays a dominant role in the recombination of devices with such back contact.

Several elements such as Tungsten (W), Molybdenum (Mo), Chromium (Cr), Tantalum (Ta), Niobium (Nb), Titanium (Ti), Manganese (Mn), Gold (Au) and Nickle (Ni) have been reported as the possible back contact materials [39, 45, 46]. Among these elements, the highest efficiency has been reported for solar cell with Mo back contact (19.9% efficiency and 81.2% fill factor) [47]. It has been very well studied and reported that deposition of CIGS on Mo creates an intermediate layer of MoSe2 at their interface. This layer makes a low resistive ohmic contact between CIGS and Mo [48, 49].

Absorber Layer

As explained in Section 2.1, the main layer in a solar cell is the absorber. The material used in the absorber layer should have the ability to absorb as much of the solar spectrum as possible to generate the most photocurrent. Lower band gap of the absorber results in the absorption of photons with a higher range of energies. However, too low of a band gap results in a low electric field, lower force to separate electron hole pairs and higher recombination rate. Therefore neither too low nor too high band gap is desired for the absorber. Figure 2.6 shows the calculated efficiency limit in Air Mass 1.5 (AM1.5) spectrum as a function of absorber band gap. As this figure indicates, the maximum theoretical efficiency of a solar cell with a single band gap absorber, belongs to the band gap range of 1.1 to 1.5 ev, with an optimum value of 33% for a band gap of 1.4 ev.

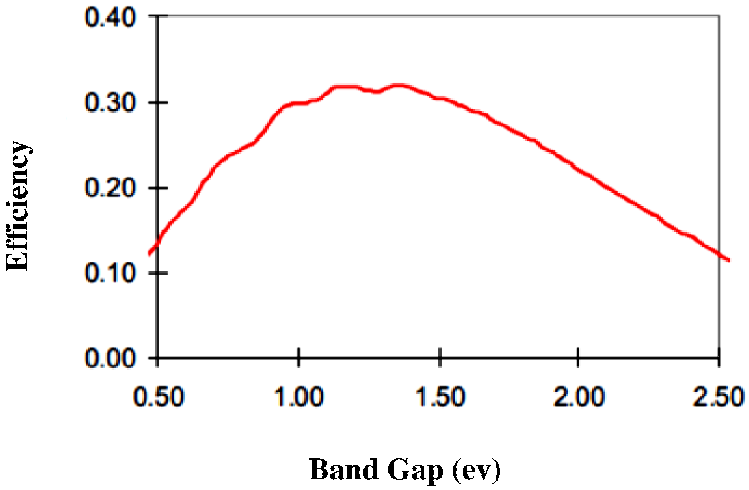

Fig. 2.6 Efficiency limitation for various band gaps of single band gap solar cells [31].

Solar cells fabricated from chemicals with band gaps close to the optimum value have been widely reported. Gallium Arsenide (GaAs), Cadmium Telluride(CdTe), Indium Phosphide (InP), and Copper Indium Sulfide ($CuInS_2$) with efficiencies of 26.1%, 16.7%, and 22.1%, respectively, are some examples of such chemicals [50].

As explained in Section 2.3, CIGS is a semiconductor with a suitable bandgap for solar absorption. Production of CIGS nanoparticles gives the ability to reduce the thickness of absorber layer, giving the potential of fabricating flexible thin film solar cells.

Buffer Layers

Any layer that is placed between absorber and front contact is called Buffer layer. The material chosen for the buffer layer should make a good junction partnership with p-type CIGS, provide low interface defects, and reduce the leakage possibility. Therefore, the buffer layer should be chosen from n-type or intrinsic materials with good lattice match to CIGS. On the other hand, the buffer layer should absorb as few photons as possible, making the materials with a wide band gap better candidates. Electron affinity (χ) is another important criterion for the selection of buffer layer. The difference in electron affinity of CIGS and the buffer layer causes discontinuity in the conduction band (ΔE_c). Too high or too low could introduce a barrier for transportation of generated electrons or increase interface recombination, respectively [24] (see Figure 2.1).

Several chemicals for buffer layers have been studied in literature [51–53]. Cadmium Sulfide (CdS) is an n-type material with a good lattice matching with CIGS. The within optimal range ΔE_c of CIGS and CdS lets a good portion of generated carriers to be transferred from absorber layer to the buffer layer [25, 54]. The problem with CdS is its bandgap of 2.4 ev, which means absorption of wavelengths below 520 nm. The light absorption by CdS could be decreased by reducing its thickness. But a thin CdS layer increases the possibility of connection between front and back contacts and production of a highly conductive shunt path. In order to reduce such a possibility, usually an intrinsic buffer layer is deposited on top of n-type CdS. Such a layer should have a high band gap and be transparent. Furthermore, since it is intrinsic, it should be thin enough not to act as a barrier for the transportation of

carriers. Intrinsic Zinc Oxide (i-ZnO) is a good candidate for such a layer, due to its high band gap of 3.3 ev and transparency. The effect of i-ZnO in shunt prevention has been studied in detail elsewhere [30].

Front Contact

The last layer in a general solar cell is transparent conductive oxide(TCO). Similar to the buffer layer, TCO should absorb the least portion of solar photons and allow the light to get to the lower layers with minimum loss. In addition, the main role of TCO is to collect the electrons generated in absorber, pass them through buffer layers, and transfer them to flow in the circuit. Therefore TCO has to have high conductivity (σ) and a low light absorption constant (α). Tin-doped Indium Oxide (In_2SnO_3) and Aluminium-doped Zinc Oxide(AlZnO) with band gaps of about 4ev and 3.3ev are the most commonly used TCOs in thin film solar cells. Both of these materials are known as highly n-doped chemicals with high conductivity. The current collected by TCO is later gathered by a metallic mesh (usually a compound of Aluminium and Nickel) deposited on top of it. In order to reduce reflection from the surface of the solar cell, it is coated with an anti-reflecting layer at the end.

3. EXPERIMENTAL

3.1 Synthesis, Purification, and Analysis of CIGS Nanoparticles

In order to synthesis CIGS chalcopyrite nanoparticles with the final molar ratio of 1:0.7:0.3:2 for Copper, Gallium, Indium, and Selenium, respectively, 0.198 g copper chloride (CuCl), 0.310 g indium chloride (InCl3), 0.105 g gallium chloride (GaCl3), and 0.316 g elemental selenium (Se)were used. The raw chemicals were poured into a 250 ml three neck flask under Nitrogen atmosphere. 25 ml Oleylamine(OLA), was added to the flask and the mixture was heated at 60°C for an hour. The temperature was then increased to 110°C while the solution was stirred and nitrogen was bubbled continuously for an hour (Figure 3.1). After an hour, nitrogen bubbling was stopped and the temperature was increased to 240°C to bake the solution for four hours under vacuum. The smoke raised from the solution was collected in a condensing column. During the whole synthesis the solution was stirred continuously to prevent the formation of large grains or undesired compounds.

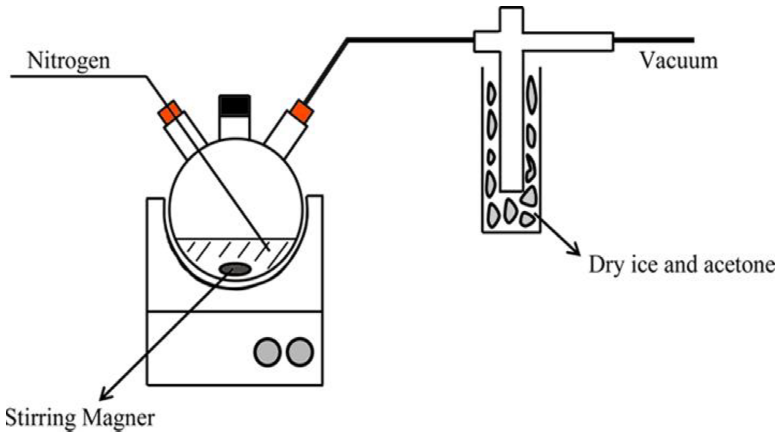

Fig. 3.1 Schematic depicting the CIGS synthesis setup

After four hours of baking, the solution was cooled down to room temperature, while covered. It was then poured in two centrifuge tubes (about 12 ml solution in each tube). Ethanol was added to the synthesised solution with the ratio of 2:1 and vortexed at 600 rpm for 5 minutes. Then the solution was centrifuged at 12,000 rpm for 10 minutes. The centrifugation of particles in ethanol at such a high speed allows particles separation from OLA. The supernatant, which included most of the used OLA, was thrown out and the precipitant, which consisted CIGS particles and any solid by-products, was kept in the tube. This process was done twice to remove all of the remaining OLA.

In order to separate the small particles from large grains and by-products, 10 ml chloroform was added to the precipitant in each tube and sonicated for 5 minutes to be well suspended. The solution was then centrifuged for 5 minutes to achieve the smallest size particles dissolved as supernatant. The byproducts and too large grains settled as precipitant. The higher the speed of centrifuge was the smaller sized particles were received. Nanoparticles with diameter less than 100 nm were achieved by centrifuging at 5000 rpm. The particles were kept in chloroform for film deposition.

3.2 Film Deposition and Analysis

3.2.1 Molybdenum Back Contact

As back contact, a layer of Molybdenum was deposited on 1 mm thick soda lime glass by a Magnetic Sputtering technique. In order to achieve a hard, smooth, and durable layer, the glass substrate was sonicated in ethanol and dried prior to being mounted in the chamber. The Molybdenum source was a 2 inches diameter sputtering target, purchased from Kurt J. Lesker company. Sputtering deposition was done with a flow of 14.1 sccm, argon pressure of 3 mtorr, and base pressure of 10^{-6} torr. The deposition rate was approximately 100 nm per second, resulting in a layer of 300 to 400 nm thick after a 5 to 6.5 minutes deposition. According to [55] it was expected to result in sheet resistance of 0.2 to 0.26 Ω/square for this layer.

3.2.2 CIGS Absorber layer

Several methods were used to deposit the CIGS layer. These methods include: Drop-casting, Doctor Blade, Spin-coating, and Spray-coating. Solutions of CIGS in three different solvents of water, chloroform, and ethanol were tried in these approaches.

Drop-casting did not give desired uniformity. Therefore, doctor Blade technique was used to modify the dropcasted CIGS on the substrate. In order to speed up the process and increase control over the film profile, the solution had to be made in a solvent with a low evaporation point, such as ethanol. To mask and apply CIGS with this technique thin tapes were adjusted in parallel on the substrate, leaving an empty rode in between. CIGS solution, were the CIGS amount was more than the open volume between the tapes, was dropcasted on one side of the rode. Then, with the help of a hard and even object, CIGS was rolled to produce a uniform film with a height equal to the tape's height. The tapes were later taken out, leaving a uniform film of CIGS.

In the spin coating technique, a solution of 0.025gr PSS in 4ml water was made and mixed with isopropanol(IPA) with 1:1 volume ratio. CIGS nanoparticles were centrifuged in ethanol at 3000 rpm, leaving pure particles at the bottom of the centrifuge tube. The PSS-water/IPA solution was later added to the pure particles and sonicated for 15 minutes. In order to spin coat a thin film of CIGS on Mo-coated glass this process was repeated 10 times: the substrate was cleaned with acetone, ethanol, and DI water, the substrate was placed in spin coater, the whole substrate was covered with CIGS solution, the spin-coater was allowed to run at 400rpm for 5min, its speed was increased to 800 for 1min, the substrate was heated on a hot plate at 300C for 5min, left to cool down for 1 min.

In the spray-coating process, CIGS nanoparticles dissolved in ethanol were sprayed onto the substrate via an airbrush. Similar to the other deposition techniques, prior to deposition the substrate was cleaned with acetone, ethanol, water and then dried.

The substrate was heated before the initial step and after each single sprayed layer at 200°C for 2 min. This process was repeated 15-20 times, depending on size of particles, the uniformity and thickness of each layer and the desired final thickness. The final product was later baked at 120°C for 12 hours. The longer the sample was heated after each and final layer, the harder the CIGS film would be, making a strong and stable layer for the next deposition step (CBD). According to morphological features of highest efficiency CIGS solar cells, post annealing the CIGS layer causes the separate particles to sinter and form large crystalline grain in the size of the film thickness [56] [57].

3.2.3 Cadmium Sulfide Buffer layer

The n side of the pn junction of CIGS solar cells fabricated in this project was a layer of Cadmium Sulfide (CdS). On one hand, the CdS layer should be very thin to transmit light to the underneath CIGS; on the other hand, it should be thick enough to guarantee the existence of a CdS layer across the whole CIGS to prevent any holes and the formation of shunt resistance.

Three different ways of drop-casting, spin-coating, settling in the solution, and chemical bath deposition were investigated. In drop-casting, some droplets of a dilute CdS solution in IPA was deposited on the substrate. Spin-coating of CdS was done in a process similar to CIGS coating, except that since CdS was dispersed in IPA, it was drying faster than the CIGS solution. Therefore, the spinning time for the initial 400 rpm was reduced to 1 min. In addition, the substrate was cooled for 2 min after each deposition. To get a thin layer of CdS, only 2 layers were spin deposited. In settling in the solution, a dilute solution of CdS in IPA was prepared. Then the substrate was soaked in the solution for a few minutes. The solution was then sucked out of the container, leaving the substrate and a thin layer of CdS on top of it. Depending on the concentration of the solution, the thickness of settled CdS varied. Compared to

Chemical Bath Deposition, neither of these techniques resulted in a thin and continues CdS layer.

Chemical Bath Deposition (CBD) CdS started by dissolving 0.75g Thiourea, $SC(NH_2)_2$, in 20ml milli-q water (0.49 Molar). In a separate container 0.17g Cadmium Sulphate $CdSO_4$ was well dissolved in a solution of 1.5ml Ammonium Hydroxide NH_4OH and 20ml milli-q water (0.037 Molar $CdSO_4$). The two solutions were then mixed on hot plate at 90° while the solution was stirred continuously. The substrate with layers of Molybdenum and CIGS was then soaked in the solution to deposit CdS on top of it. At the end, the substrate was washed with harsh flow of DI and milli-q water. In order to investigate the effect of time on the thickness and continuity of the film this process was repeated for different timings, from 3 to 25 min.

3.2.4 Intrinsic Zinc Oxide Buffer and Aluminium Doped Zinc Oxide Front Contact Layers

Different techniques of drop-casting, spin-coating, dip-coating, and spraying were investigated to deposit thin, uniform, and transparent layers of intrinsic zinc oxide buffer and aluminium-doped zinc oxide back contact layers.

In drop-casting intrinsic and aluminum-doped ZnO, solutions of these materials in IPA with different concentrations were used. However, none resulted in a continuous layer. Spin coating looked more promising in continuity, but it did not result in uniform transparency. The solution that was used for spin coating was made of 0.05 g ZnO in 4 ml isopropanol, sonicated for at least 30 min. Dip-coating was another technique that was explored to yield the thinnest layer of ZnO (specially the intrinsic type) possible. A dilute solution of ZnO in IPA was prepared and the sample was dipped in the solution horizontally. Then the sample was put aside at a small slip angle to dry out. It was later heated to harden the deposited layer. Although this technique is easy to apply, it rarely resulted in a transparent film, the continuity and thickness of the film highly depended on the experiment's physical parameters.

Spray coating the last technique used for deposition of ZnO layers. In this technique, solutions of 0.1 g i-ZnO and 0.2 g Al-ZnO in 4ml ethanol were sonicated for at least two hours and then sprayed on the sample. The sprayer used for this process was a Paasche VLS-SET Double Action Siphon Feed Airbrush. Although this technique resulted in high roughness of the deposited layer, it was preferred to the other techniques due to higher controlability on the thickness and transparency of the deposited layer. It is believed that the thickness and transparency of the film can be further improved by using a more modern sprayer with smaller size shot droplets. In a similar experiment, the spray deposition was applied while the sample was moving uniformly. Here, the same solution and procedure was applied to the sample spinning at speed of 200 rpm.

3.3 Solar Cell Device Fabrication

This section explains the fabrication methods used to assemble solar cells from the deposited films in the previous section.

The devices explained in this section were fabricated by deposition of each layer on top of the other, from the front contact to the bottom contact(type B: Top Down) and from the back contact to the front contact(type A: Bottom-Up).

Type A: Bottom-Up

Type A or Bottom-Up devices were fabricated on a single substrate consisted of the deposition of layers on top of each other, starting from the back contact. This naming can be clarified by referring to Figure 2.5, where the back contact is placed at the lowest level and the other layers are mounted on it.

In this process, the Molybdenum (Mo) back contact layer was deposited first, following CIGS, buffer layers, and Al-ZnO. Before the deposition of Mo the substrate was cleaned with ethanol and sonicated for 30 min. After Molybdenum was deposited, the substrate was gently cleaned with acetone. A CIGS film of 0.4 to higher than 1 μm

thick was deposited on Mo, depending on the deposition technique and the desired thickness. The sample was annealed at 200°C over night to providing hardening and increasing the grain size as explained in Section 3.2.2. 300 nm thick CdS, 1.5 μm thick i-ZnO (in some samples this layer was skipped for transparency and conductance improvement), and 1.5 μm thick n-ZnO films were deposited one after the other. The final device was post annealed at 200°C for two hours. At the end, a droplet of silver paint was deposited on the a thick area of n-ZnO for current collection purposes. Note that before each spray deposition the sample was covered by a mask to reduce the shortening possibility and increase the shunt resistance.

Type B: Top-Down

Type B or Top-Down devices were fabricated by deposition of layers starting from the front contact to the back contact (Figure 2.5). N-ZnO or ITO was chosen as the front contact and first layer in type B devices. In either case a transparent layer of the front contact was deposited on soda lime glass. n-ZnO was spray-deposited while ITO-coated glass was purchased commercially. The front contact was followed by the spray deposition of a thin layer of i-ZnO (in some devices this layer was skipped) and CBD of CdS. A 2 μm CIGS absorber layer was then spray deposited on the top followed by annealing at 200°C overnight to harden the layers and prepare them for back contact deposition. The sample was then masked for deposition of the Mo back contact. The sample was placed in the sputtering chamber at the highest distance from the sample to reduce the diffusion of Molybdenum into the CIGS layer.

The pros on "Single Substrate" processes is that all the layers are deposited on top of each other, covering the roughness of the previous ones accordingly. This improves the contact of the layers, increasing the interface area and conduction ability. For the same reason, if there are any cracks or holes in any of the mid-layers of Single Substrate devices, the upper and lower layers can touch each other, decreasing the shunt resistance. Theoretically, this problem should be less probable in type B devices,

as the buffer layer is covering the front contact with low roughness, decreasing hills and valleys on the surface of buffer layer. However, sputtering of Mo on the other side of CIGS increases the possibility of shortening. The harsh bombardment of Mo can destroy the CIGS surface and diffuse into the buffer and front contact layers, decreasing the shunt resistance. This possibility could be reduced by using alternative gentle deposition techniques for deposition of back contact.

4. RESULTS AND DISCUSSIONS

4.1 CIGS Nanoparticles

4.1.1 Nanoparticles Analysis Using SEM

This section shows the characterization and analysis of the synthesized nanoparticles. As explained in the previous chapter, the synthesis was performed in Oleylamine (OLA). Therefore the output particles were coated with OLA, which had to be removed to get full functionality. The removal process in ethanol and chloroform was explained in detail in the previous chapter. Figure 4.1 compares Scanning Electron Microscopy (SEM) images of nanoparticles before and after the cleaning process. The left SEM image displays particles immediately after synthesis (before cleaning) while the one on the right shows particles after the cleaning process. The middle image shows a mid cleaning process stage, where most of OLA has been washed away but the particles still look oily. The cleaner particles display clearer edges and are more distinguishable in the images.

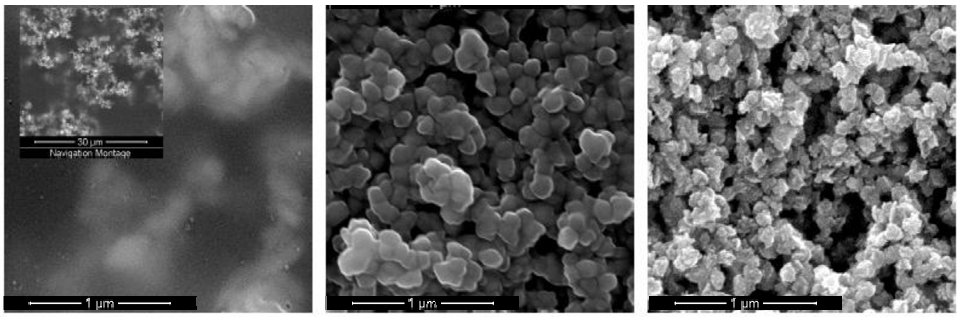

Fig. 4.1 SEM images of synthesized nanoparticles. Left: before, center: intermediate, and right: after cleaning processes. OLA on the particles was washed away through cleaning processes.

After cleaning, the particles were purified and separated based on their sizes. Figure 4.2 compares SEM images of the particles before and after purification, without considering size. The impurities and byproducts in the left image are erased after purification in the right image.

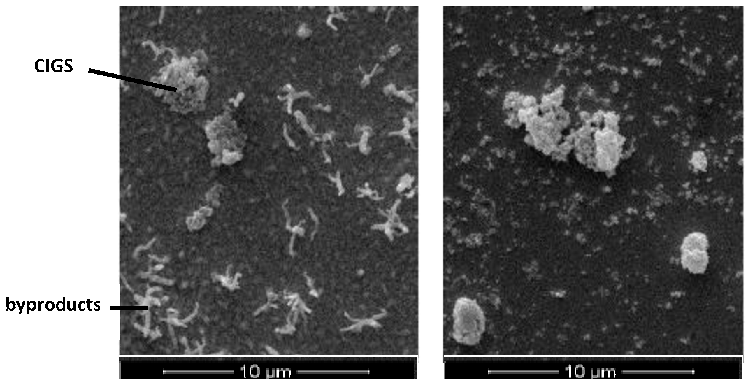

Fig. 4.2 SEM images of synthesized and cleaned nanoparticles. Left: before, and right: after purification. The byproducts and impurities are cleaned.

In the purification process, the higher the centrifuge speed was, the smaller the particles obtained. Figure 4.3 shows SEM images and the size distribution of the purified particles. As shown, the higher the centrifuge speed was, the lower size of particles were achieved. In this graph, the smallest particles are labeled as "Grade 1" and the "Grade" number increases as the size increases. Grade 1 particles had average diameter of 91 nm obtained at a 5000 rpm centrifuge speed, while smaller particles could be achieved by increasing the centrifugation speed. It was observed that smaller particles resulted in more uniform CIGS film with lower film surface roughness. However, bigger particles also gave films with acceptable roughness and thickness. Smaller particles could be used for the fabrication of thinner solar cells, yet the efficiency of the solar cell decreases for too thin devices. The optimum thickness of the CIGS layer will be explained in Section 4.3 in detail.

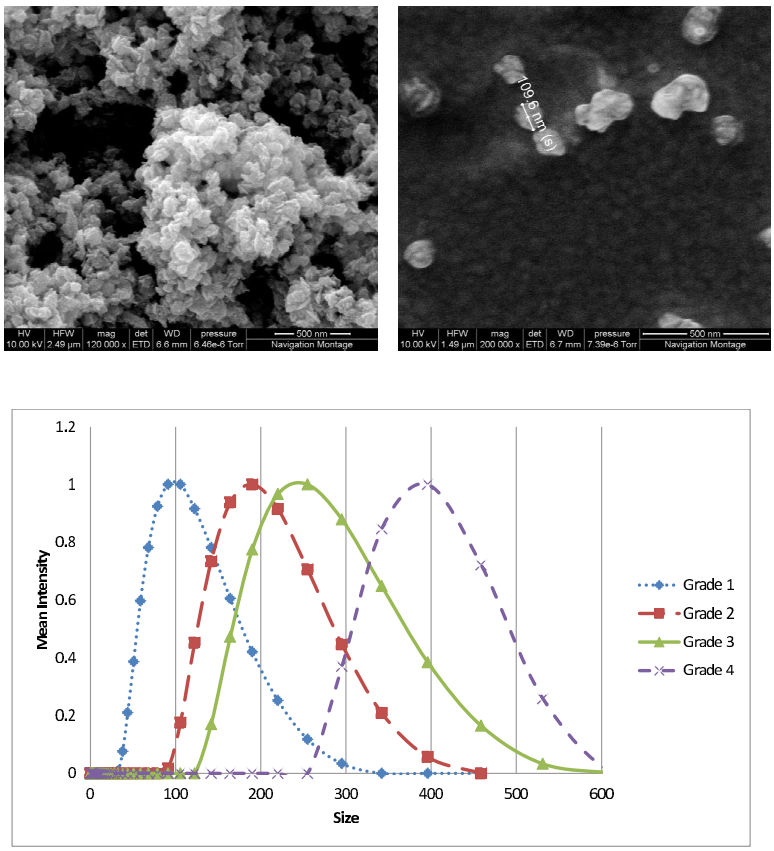

Fig. 4.3 Top: SEM images of nanoparticles. Bottom: Size distribution of a solution of nanoparticles in chloroform

4.1.2 Elemental Composition and Crystallography

In order to make sure the nanoparticles have all four elements of Copper, Indium, Gallium and Selenium, Energy-dispersive X-ray spectroscopy (EDS) of several nanoparticles were taken. Figure 4.4 shows the EDS of a sample nanoparticle on gold coated silicon substrate. This figure and similar results for different bulk and nano-sized particles confirm the presence of all four elements in synthesised CIGS. Even though EDS was used only to investigate the types of elements in the nanoparticles, the ratio of the elements in both bulk area (about 100 μm) and nano-sized particles were very close with some variations in the Ga and In portions.

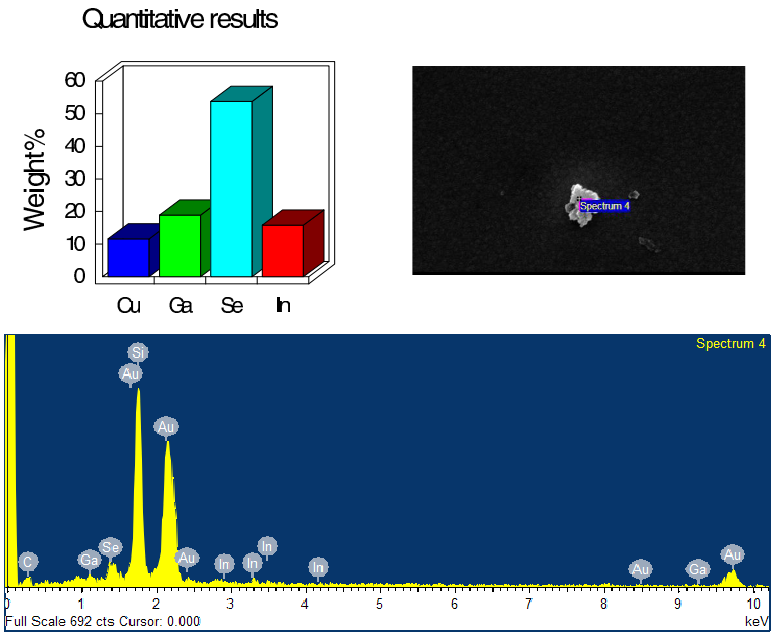

Fig. 4.4 A sample EDS of a nanoparticle showing the presence of all four Cu, In, Ga, and Se elements

Although EDS verifys the types of elements included in an area, it does not give information about the crystalline structure of the particles. X-ray Diffraction (XRD) was used to investigate the crystal structure of the nanoparticles. The XRD pattern peaks at the planes of the crystal's structure represent a 3D image (Figure 2.4). Figure 4.5 shows the XRD pattern of CIGS nanoparticles synthesised in this project. The diffraction had major peaks at 26.18°, 43.88°, 52.14°, and 64.4° of 2θ angle representing (112), (204)/(220), (116)/(312), and (400)/(008) planes of the tetragonal crystal structure of CIGS. The minor peaks at 27.22° and 35.16° 2θ represented (103) and (211) planes, distinguishing the chalcopyrite from sphalerite structure, were also observed.

4.1.3 Absorbance and Band Gap

Another important parameter in CIGS nanoparticles that had to be tested and analysed was light absorption. Light absorption gives information about the ability

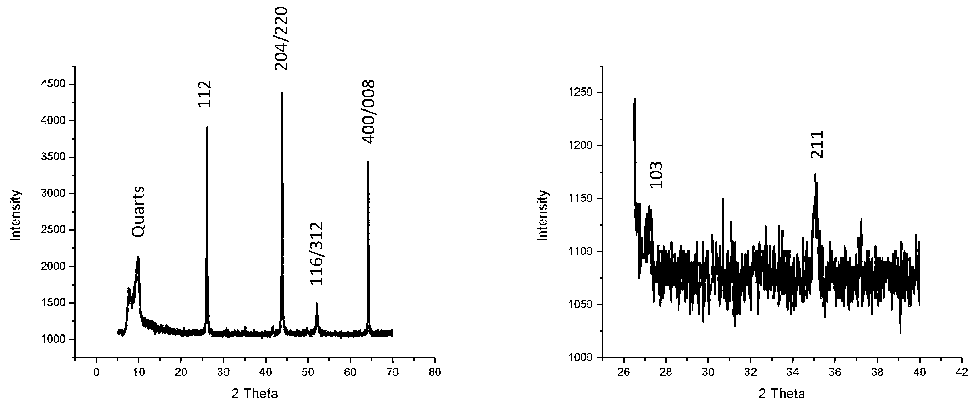

Fig. 4.5 X-ray Diffraction pattern of CIGS nanoparticles. Left: the major peaks confirming the tetragonal structure while right: the minor peaks confirm the chalchopyrite structure

of a material to be used as absorber layer in a solar cell. The response of our CIGS nanoparticles to ultraviolet, visible, and near infra-red spectrum were measured in both dispersed in a liquid (such as chloroform) and as a dried dropcasted layer. Both provided similar results. Figure 4.6 shows the particles' capability of absorbing photons with wavelengths ranging from 300 to 1300 nm. The maximum observed absorption was between 300 to 600 nm, which aligns with the solar spectrum of 350 to 750 nm.

The Band gap of the nanoparticles can be found from their response to light. As indicated in Chapter 2, electrons need to absorb energy at least equal to their band gap in order to jump from the valance band to the conduction band and contribute in current conduction. Therefore, the least amount of energy or highest absorbed light wavelength leads to the calculation of band gap. According to Tauc's relationship, for direct band gap semiconductors the band gap relates to the absorption coefficient, α, by

$$\alpha h\nu = A(h\nu - E_g)^{\frac{1}{2}} \tag{4.1}$$

where $(h\nu)$ is the photon energy, E_g is the band-gap, and A is a constant [21]. Therefore, plotting $(\alpha h\nu)^2$ versus photon energy gives the band-gap on the cross section

point of the energy axis and the tangent of the plot's linear section's. Figure 4.6 indicates the band-gap of synthesized CIGS nanoparticles is around 1.33 ev. This band gap can be tuned by varying the initial Gallium to Indium ratio of raw materials before the synthesis.

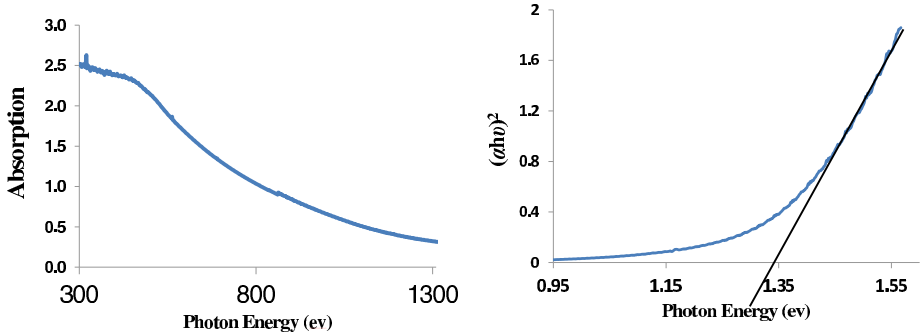

Fig. 4.6 Left: Light absorption of nanoparticles dispersed in chloroform, right: calculating the band gap of CIGS nanoparticles by Equation 4.1

4.2 Film Depositions

4.2.1 CIGS Film

CIGS nanoparticles dispersed in ethanol were sprayed deposited onto a substrate for thin film for solar cell application. The characteristics of this film, such as its surface roughness, thickness, and response to light were studied and analyzed. Roughness and thickness were quantified using Atomic Force Microscopy (AFM), while light effects were measured by studying the current-voltage characteristics of the film before and after being exposed to light illumination.

Analysis of the surface of a thin film CIGS using AFM showed a uniform film with uniform hills spreading along the surface. These hills had a height of about 70 nm from the CIGS valleys with an average distance of less than 1 μm from each other. The height of the hills can be changed by manipulating the sprayer's pressure

and its distance from the substrate during deposition. These parameters also affect the uniformity of the hills spread along the surface. Figure 4.7 shows the surface morphology of the CIGS film, the approximate distance of the hills from each other, and the average hill height.

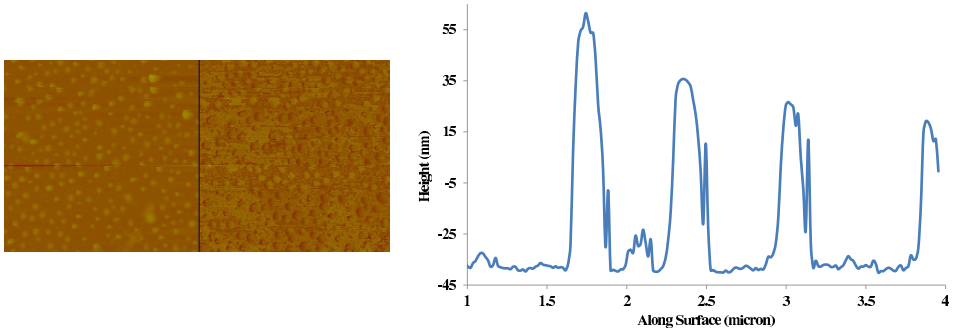

Fig. 4.7 Left: 2D and 3D AFM images of a CIGS film sprayed on plain glass, right: analysis of the height along the surface

The thickness of CIGS film was also measured by AFM. In order to achieve this parameter, a 7 μm wide scratch was made on the film by a sharp pin. The difference between the average height of the area inside the scratch and on the film surface was taken as the film thickness. The creation of a scratch on the continuous film caused the CIGS material on the scratch area to move to the boarder of the scratch. Therefore, in order to have an accurate height measurement, the height difference was taken as the difference of the area inside the scratch and film surface area far from the scratch. Figure 4.8 represents an image of the explained scratch on the CIGS film and measurement of the thickness. This measurement indicated about 400 μm thick film, while this value could be controlled and changed by the spray deposition of more or less material.

In order to make sure the scratch from metallic pin did not alter the glass substrate, the same procedure was done on bare glass. No scratch was made on the bare glass, indicating that the procedure did not deepen the normal height of the glass substrate.

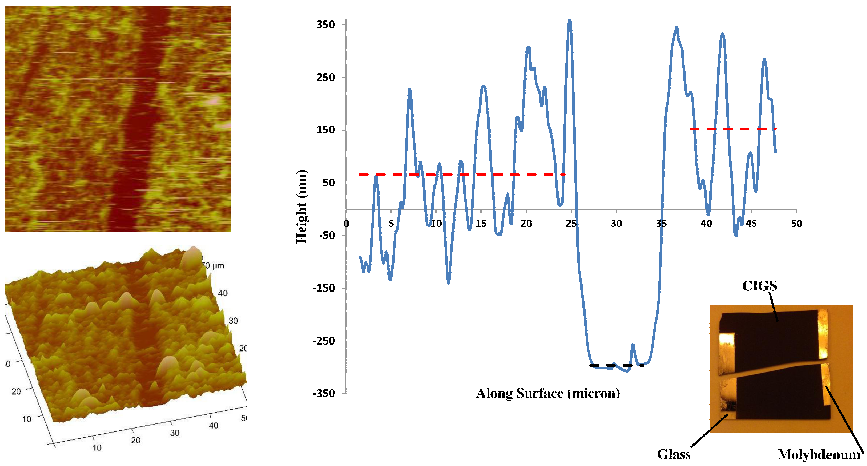

Fig. 4.8 Left: 2D and 3D AFM image of a CIGS film and a scratch used to measure the thickness. Right: Analysis of the height along the surface. Image: Film of CIGS sprayed on Molybdenum coated glass

Other than the number of spray depositions, it was observed that the distance of the airbrush and its shooting speed strongly affect the thickness and roughness of the deposited film. The farther the distance, the thinner the film and lower the roughness. Similarly, the lower the shooting speed the more uniform, thin and smooth the film. These parameters give higher controllability over the morphology of the film. Modifying these parameters by computer can lower the material usage even further and improve the film's structure.

Other than the morphology of the CIGS film, its response to light illumination was also studied. This experiment was done by depositing a film of CIGS between two conductive probes. The conductivity of the channel was tested by measuring current-voltage characteristic via a Keithley 4200SCS instrument. Two straight lines in Figure 4.9 represent the resistance of CIGS film in darkness and under light illumination. The zigzag line shows the current value at unit voltage values when the film was exposed to light and at half unit voltage values when it was located in darkness. The time difference between each point of this zigzag line was 2 sec, verifying the fast response to the light illumination (note that the minimum required time for such

response was not measured). This graph indicates that the resistance of the CIGS film decreased when it was exposed to light and increased when the light was taken away.

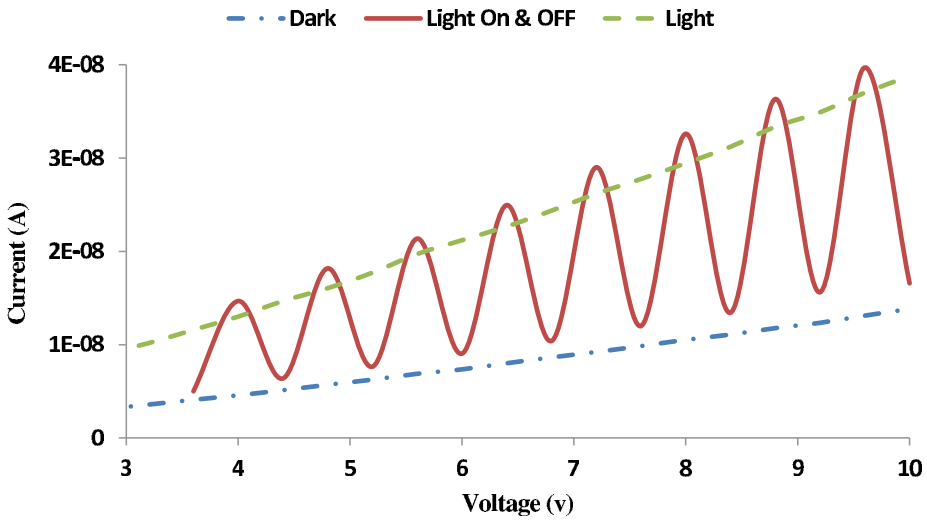

Fig. 4.9 Current voltage characteristic of a channel of CIGS nanoparticles deposited on glass slide

4.2.2 Effect of Post Annealing

As it was discussed in Section 2.3, vacancy of Cu results in the formation of p-type CIGS while Se vacancy transfers it to an n-type material. It was observed that annealing the CIGS film at temperatures higher than 250 degree centigrade results in evaporation of Selenium (which is the main reason for post annealing under selenium vapor - known as selenization process - reported in most literature). The effect of post annealing was viewed by comparing the light effect on the CIGS channel. Table 4.1 compares the ratio of resistance of the film under light illumination and darkness for different post annealing temperatures. This experiment confirmed that post annealing improves conductivity. However, since selenium was evaporated at high temperatures the CIGS film changed its characteristics and its response to light was highly reduced.

Table 4.1 Effect of post annealing (under air atmosphere) on the response of CIGS film to light illumination

Temperature	**70°C**	**150°C**	**250°C**	**350°C**	**450°C**
$\frac{Resistanceunderillumination}{Resistanceindark}$	0.555	0.357	0.435	0.909	0.952

4.2.3 CdS and ZnO Films

In order to observe the functionality of synthesized CIGS nanoparticles as a thin film in a solar cell, buffer and front contact layers also needed to be deposited. The deposition of CdS as an n-type buffer layer was done via a Chemical Bath Deposition process (see details in Section 3.2.3). The thickness of this layer could be controlled by either modifying the ratio of the initial materials or by changing the deposition time. The longer the deposition time, the thicker CdS layer would be deposited. This layer had to be thick enough to ensure it covered all pores of the CIGS layer underneath. It also had to be thin enough to absorb the least amount of light photons and transparent them to the underlying CIGS layer. It was observed that with the raw material ratios reported in Section 3.2.3, deposition for 5 minutes or more resulted in a yellow layer viewable by bare eyes. AFM was performed on CdS films with various deposition times to analyse thickness. The deposition time of 2 to 4 minu resulted in films with a thickness of about 300 to 800 nm, while 1 min deposition did not result in a continuous and uniform film (Figure 4.10).

Intrinsic and aluminium doped ZnO layers were to be deposited as the second buffer and front contact, respectively. The deposition of these two layers were done via spray deposition (similar to the deposition of CIGS) and simultaneous spin and spray (SS). These two layers had to be continuous, thin and transparent to absorb the least amount of light. Spray deposition did not result in high transparent films. However, the films had high roughness and thickness. SS deposition resulted in more uniform, smooth and transparent film, and is worthy of further study. The purpose

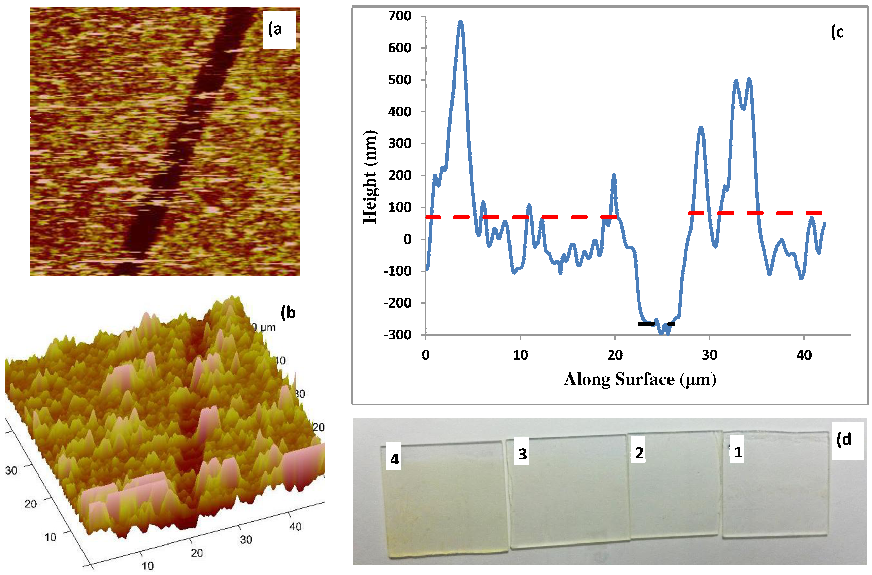

Fig. 4.10 a)2D AFM image, b)3D AFM image, c)Analysis of the height of CdS film deposited for 2 minutes. d)image of CdS films deposited for 1 to 4 minutes

of spinning is to give a continuous movement to the shot droplets and make them to lay and spread on the substrate instead of sitting horizontally. This movement could be of any uniform type, including rotational or linear. Figure 4.11 compares the transparency, and roughness of these two methods for deposition of ZnO. AFM images of the two films showed roughnesses of about 1000 and 500 nm, and average thicknesses of 1500 and 800 nm for ZnO films deposited on glass via Spray and SS methods, respectively. Both of these deposition methods are low cost and highly scalable.

4.3 Solar Cell Device

4.3.1 Simulation Results

This section shows the simulation results of a device made of films with properties similar to what was fabricated experimentally. Effects of the physical parameters of such cells were studied theoretically using ADEPT 2.0 simulator. ADEPT 2.0 is a

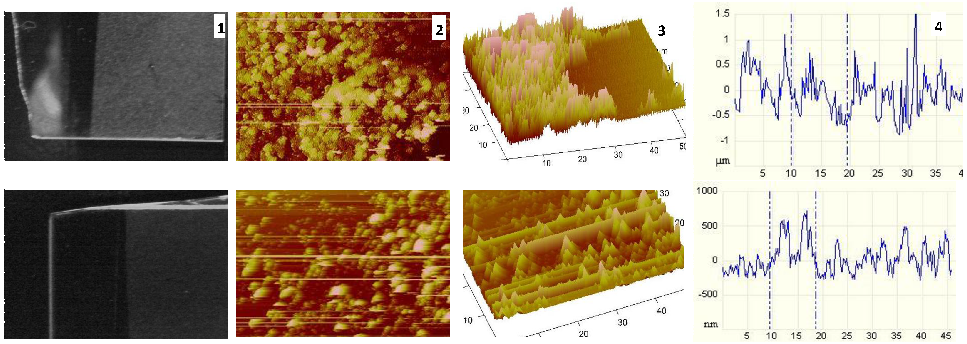

Fig. 4.11 Film of ZnO deposited via Top: Spray deposition, Bottom: Spin and Spray (SS) simultaneously. 1)Image taken by camera showing the transparency and uniformity, 2)2D AFM image of the surface, 3)3D AFM image, 4)analysis of the surface roughness

simulator software that was originally made to model the semiconductor behavior of solar cells. The simulator partitions the sample to meshes and solves the transport equations (see Section 2.2.1) discretely for each mesh. Then it solves sets of coupled non-linear equations using a generalized Newton iteration method. Therefore, the simulator inputs the total number and spacing of nodes for mesh specifications as well as maximum number of iterations and maximum error for Newton method's convergence. ADEPT 2.0 was run from the nanoHUB.org website of Purdue University [58].

The physical parameters that were used for simulation are presented in Appendix B. The parameters used for intrinsic zinc oxide were almost the same as what was used for n-doped zinc oxide, except the the dielectric constant and doping density with values of 7 and $2 \times 10^{17} cm^{-3}$, respectively. The simulated parameters via this software included the effects of layer thickness, CIGS doping density, and light spectrum and intensity.

Thickness

On one hand, the thinner the absorber layer is, the less material would be needed and the lighter device fabricated. Furthermore, too thick of a layer can increase series

resistance and decrease conductivity. On the other hand, too thin absorber layer will result in the generation of electron holes close to back contact, where the back contact recombination happens [36, 59].

As the first step, the thickness of the CIGS layer was simulated to find an optimum value that resulted in thin and high efficient solar cells. The studied thickness varied from 0.1 to 10 micron (Figure 4.12). The decrease in Quantum Efficiency (QE) of the thinner film cases could be due to the high back contact recombination. This effect is more noticeable for long wavelengths since only this portion of the spectrum penetrates through the CIGS and makes the electron hole pairs deep inside the absorber [60]. Therefore, for the devices with thinner absorber layers the electron holes generated by these wavelengths recombine before contribute into the photo current (for more information about back contact recombination as surface recombination please refer to Appendix A). Due to low QE, the generation current (I_L) is much lower in thin CIGS film devices than the ones with thicker films (see Equation 2.25). Lower generation current means lower overall current (Equation 2.27). Furthermore, according to Equation 2.29 lower generation current results in lower open circuit voltage. Therefore, as a CIGS layer gets thicker, the overall efficiency of the solar cell increases. This increase saturates when the thickness of the absorber layer reaches 1 μm. Hence, in order to fabricate a highly efficient device by using the least amount of material, 1 μm thickness should be considered for CIGS layer.

Absorber is not the only layer that shows thickness affects on the performance of the solar cell. CdS, which covers CIGS, has bandgap of about 2.4 ev. This means the absorption of light photons with wavelengths lower than 516 nm by CdS. This range covers a wide portion of the energetic solar spectrum where CIGS absorption is the highest. Therefore the CdS layer should be as thin as possible to absorb the least amount of light photons. But the issue is that CdS as an n-type buffer layer has to be thick enough to cover the whole rough CIGS surface. In an study, the thickness of CdS and its effect on the performance of a solar cell was simulated. As Figure 4.13 indicates, CdS of 500 nm or thicker absorbs a major portion of light

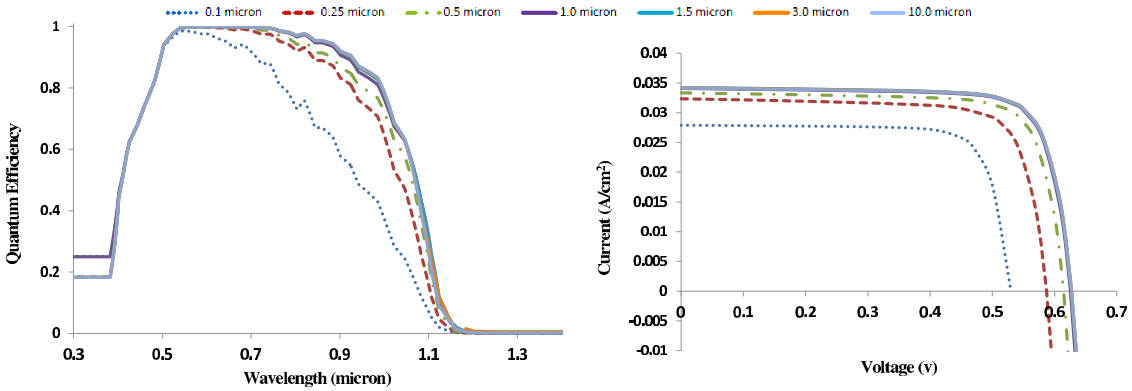

Fig. 4.12 Simulation results showing the effect of CIGS thickness on the overall solar cell performance.

with wavelengths lower than 500 nm. This reduction lowers the current generation, resulting in a reduction of the overall current.

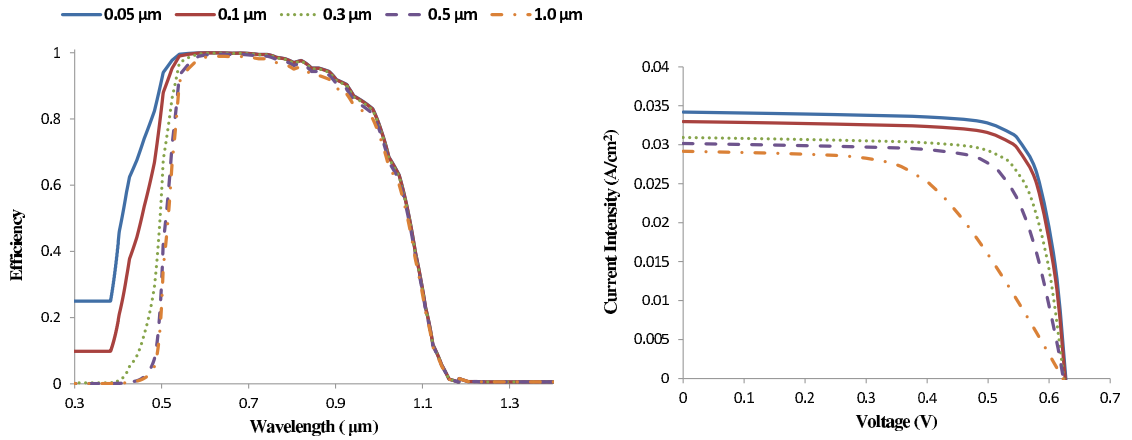

Fig. 4.13 Simulation results showing the effect of CdS thickness on the overall solar cell performance.

Doping Density

One of the main parameters that affect the functionalization of the absorber CIGS is its doping density. Since selenization process was not perused in the fabrication of this project's solar cell, the loss of Se and reduction in the acceptor properties of CIGS during annealing steps is very probable. Therefore, effect of CIGS doping density variation on the performance of the overall device was simulated. In this study, the thickness of layers was fixed as optimum values given in the appendices.

The acceptor type doping density of CIGS was lowered from 10^{16}, as the usual value reported in the literature, to 10^{12}, a value close to intrinsic case. Doping density of CdS as the n-side was kept constant, resulting in increase of the depletion region's length in the p-side CIGS (Equation 2.20) and overall pn junction width (Equation 2.19). An increase in the depletion width provides more space for generation of the electron holes that can contribute in the current conduction and results in a slight increase in the short circuit current.

Equation 2.21 indicates that reduction in the doping density causes the built in voltage to decrease. Hence, open circuit voltage, which is directly related to the built in potential, reduces as well. This theoretical explanation was clearly observed in the simulation results (Figure 4.14), where reduction of doping density from 10^{16} to 10^{12} caused a decrease in open circuit voltage from higher than 0.6 v to about 0.33 v. Open circuit voltage saturates for doping densities less than 10^{12}, where CIGS is about to change its property from p to n type.

Light Illumination

As indicated in Equations 2.24 and 2.25, the generation rate and current density are directly proportional to the illuminated light's intensity. Other than the intensity in specific wavelengths, the coverage of the whole solar spectrum is also important. If the applied lamp for testing a solar cell either does not have high enough intensity or does not cover some portion of solar spectrum the measured open circuit voltage

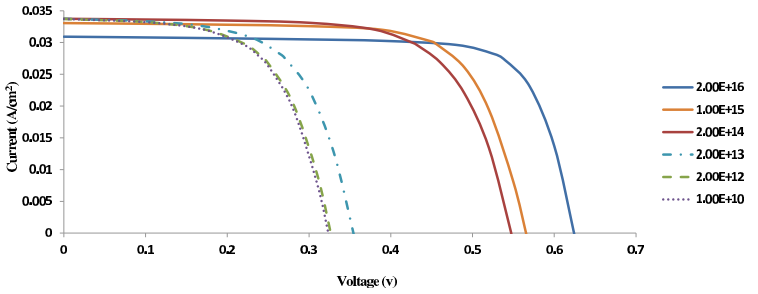

Fig. 4.14 Simulation results showing the effect of CIGS doping density on the overall solar cell performance.

and short circuit current would be significantly reduced compared to the response of the device to Air Mass 1.5 (AM1.5).

The lamps that were used in our lab for testing fabricated solar cells suffering from both of these issues. In a study, the intensity and wavelength limitations of the lab lamps were applied to the simulator. To make the simulation closer to reality, the thickness of the solar cell layers were fixed to the thickness of a real fabricated device and doping of CIGS layer was reduced to satisfy the lack of selenization. Figure 4.15 compares the performance of a device exposed to AM1.5 and lab lamp. It is clear that the current would reduce significantly, resulting in a reduction in the open circuit voltage as well.

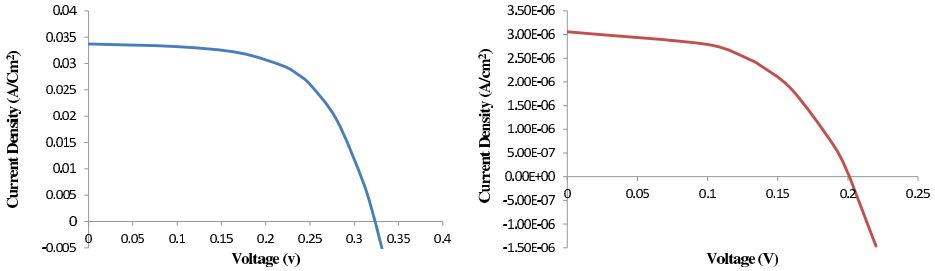

Fig. 4.15 Simulation results showing the performance of solar cell with parameters close to what fabricated in the lab under Left:AM1.5 spectrum, Right:lamp used in the lab.

4.3.2 Experimental Results

In type A (Bottom-Up) devices the CIGS nanoparticles were spray deposited on Molybdenum coated glass. CdS covered the CIGS layer via Chemical Bath Deposition, followed by spray deposition of Zinc Oxide buffer and front contacts. The CIGS thickness was about 2 μm, while the thickness of CdS and each ZnO layers were 300 nm and about 1.5 μm, respectively. At the end, a droplet of silver paint was used as a hard metallic contact for measurement purposes. In type B (Top-Down) devices, the fabrication started from front contact layer and layers were deposited down to the back contact layer. ITO was used as the front contact, followed by deposition of CdS, CIGS and Molybdenum.

Fabrication of type A resulted in a device with a 0.2 v open-circuit voltage and 0.3 $\mu A/cm^2$ short circuit current density and %30 Fill Factor. These electrical parameters are lower than the devices reported in literature due to the low transparency of the front contact layer, lack of selenization and low annealing temperature, and use of a partially covered solar spectrum lamp. However, the experimental open circuit voltage and short circuit current density were close to the simulation results of a device with similar conditions (Figure 4.16). The difference of 0.42 $\mu A/cm^2$ in J_{SC}, 0.02 v in V_{OC}, and 0.196 units in FF between the experimental and simulation resulted in an efficiency of %1.49 for experimental and %3.23 for simulated solar cells. The difference could be due to the error in simulating a thick ZnO layer. It was expected that variation in the thickness of ZnO, specially the intrinsic one, affects the current conduction and fill factor, while the simulator did not show any changes.

Fabrication of the type B device resulted in a higher short circuit current density, but much lower open circuit voltage. Overall the efficiency of top-down devices were ten times less than bottom-up devices. Other than the lower efficiency, the fabrication of top-down devices were more complicated than the bottom-up devices with lower throughput. This could be due to the sputtering of Molybdenum that had to be done

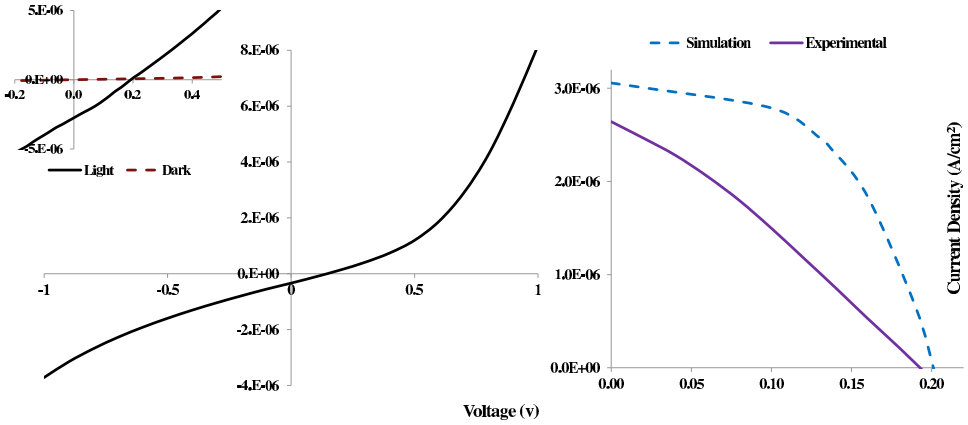

Fig. 4.16 Left: I-V characteristic of type A (Bottom-Up) solar cell fabricated and tested in the lab. Right: Comparison of experimental and simulated solar cells

at the end, which increases the risk of destroying and diffusing through the beneath layers and reducing shunt resistant.

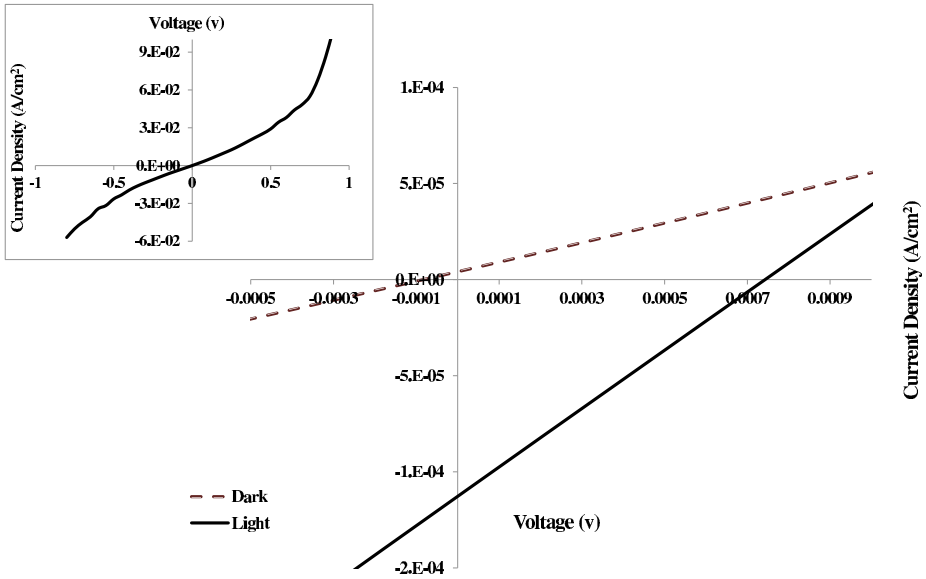

Fig. 4.17 I-V characteristic of type B (Top-Down) solar cell fabricated and tested in the lab.

5. CONCLUSIONS AND FUTURE RECOMMENDATIONS

5.1 Conclusions

Synthesis of $Cu(InGa)Se_2$ nanoparticles, their deposition into thin films, and fabrication of solar cell from the films have been presented and discussed. The presented fabrication approach uses low-cost and scalable processes that have potential for providing us with a commercially viable alternative source of energy.

$Cu(InGa)Se_2$ nanoparticles were synthesised and purified via a high throughput chemical process. Purification was confirmed based on observed SEM results. The chemical quality of the synthesized nanoparticles, including their material content and their crystal structure, were analysed via EDS and XRD, confirming the formation of tetragonal chalcopyrite of the four Cu, In, Ga, and Se elements. Light absorption was analysed by UV-Vis-NIR spectroscopy, confirming the absorption ability in the range of 300 to 1200 nm, in good alignment with the AM1.5 solar spectrum. The synthesis method utilized a chemical colloidal process resulting in the formation of nanoparticles with tunable band gap and size. Based on the theoretical and experimental study conducted, 100 nm nanoparticles with an associated band gap of 1.33 eV were selected to achieve the desired film characteristics and device performance.

Deposition of analyzed nanoparticles was performed using simple, low cost, and scalable spray-coating techniques. The thicknesses and surface roughness of the deposited films were controlled through variations in the deposition steps, substrate to spray-nozzle distance, size of the nozzle, and air pressure. The deposited films were observed to be relatively uniform with a minimum thickness of 400 nm. Current density and voltage (J/V) characteristics of 1 μm thick film were measured under light

illumination. The highest photoelectric effect was observed for the films that were post-annealed at temperatures between 150-250 °C under air atmosphere.

Effect of thickness of layers, doping density of absorber layer, and light illuminant on a solar cell was simulated by ADEPT 2.0 software. The simulated solar cell consisted of the films with properties of what was deposited in the lab. Concluding from the simulation results, solar cells with 1 to 2 μm thick CIGS and 300 nm thick CdS were fabricated in the lab. The open circuit voltage of the fabricated device was very close to the simulated results while the short circuit current density differed for 0.42 $\mu A/cm^2$. The fabricated solar cell had about 1.5% efficiency. This efficiency could be further improved by modifying the ZnO layers and making it thinner, higher transparent and more uniform. In this project Spraying while Spinning (SS) technique was reported as a low cost and scalable alternative process. Reducing the thickness of CdS can also improve the fill factor and efficiency.

The developed CIGS films along with layers of Molybdenum (Mo), Cadmium Sulfide (CdS) and Zinc Oxide (ZnO)were implemented in solar cell devices. In a typical cell, a 1 μm thick CIGS film following by a 300 nm CdS was deposited on 350 nm thick Mo layer. Mo served as back contact of the solar cell while CdS film served as the n-type layer to form a pn junction with the p-type CIGS layer. A thin layer of intrinsic ZnO was spray coated on the CdS film to prevent the shunting with the top conductor layer, 1.5 μm spray-deposited aluminum doped ZnO layer. A set of fabricated devices were tested using Keithley semiconductor characterization instrument and micromanipulator probing station. The highest device efficiency measured to be 1.49%. The considered solar cell devices were simulated in ADEPT 2.0 solar cell simulator based on the given fabrication and experimental parameters. The analysis of the simulation results confirmed the experimentally measured results.

5.2 Future Recommendations

In this work, CIGS solar cells were fabricated through the processes that do not require any post selenization. However, it was shown that post annealing even under air atmosphere improved the response of the CIGS film to the light illumination. Some literature reported that post annealing at high temperature causes the transfer of particles into large grains in the size of the film's thickness. This could increase the connectivity in the CIGS layer and at its surface contacts with CdS and Molybdenum. In order to achieve such higher connectivity of nanoparticles to each other and improve conductivity, the CIGS film should be either post annealed at the presence of selenium vapour, or it should be mixed with some other material. This material could be a polymer that increases the connectivity of CIGS nanoparticles, but does not affect their conductivity.

In order to further reduce the material waste in spray deposition, the optimum shooting speed and distance of the spray from the surface should be studied. The shooting speed could be controlled by watching the pressure of the gas inlet, while the distance can be adjusted for a fixed pressure. The size of nozzle is another parameter that can reduce the size of droplets and result in the formation of less air-gaps between the particles and use the material more efficiently.

Zinc oxide plays an important role in collecting the current from the surface of solar cell and guiding it to the metallic contacts. The transparency of this layer is a key factor in letting the most portion of light reaching the absorber layer. Surface roughness of this layer also affects the conductivity of this layer. Solely spraying did not result in a highly transparent and smooth deposition of zinc oxide. Although the thickness and surface roughness could be improved by optimizing the spray deposition's parameters, the formation of hills and valleys cannot be easily abandoned in a thin layer of ZnO. One solution could be moving the sprayer or the substrate during the spray deposition to let the droplets lay and spread on the surface. This technique

was tried in this project and gave some promising results. However, the movement speed has to be adjusted and optimized with the sprayer's parameters.

In this project, silver paint was used as the metallic contact to collect the current from the ZnO front contact and transfer it to the circuit. It is highly probable that the droplet of silver paint mounted on ZnO at a corner of the cell resulted in a loose connection. Such connection increases the resistance between the two sides and reduces the current conductivity. An alternative way to mount this electrical contact could be deposition of a very small amount of a metal in hot environment. The hot environment can melt the metal and let it to fill the roughness of the underneath layer. A metallic mesh should be made to improve the current collection.

LIST OF REFERENCES

LIST OF REFERENCES

[1] "International enrgy outlook 2011," Tech. Rep. DOE/EIA-0484(2011), US Energy Information Adminstration, September 2011.

[2] "Opec basket price," tech. rep., Organization of the Petroleum Exporting Countries, 2012. http://www.opec.org/opec_web/en/data_graphs/40.htm?selectedTab=annually. Last accessed July 2012.

[3] "Sunshot vision study," tech. rep., US Department of Energy, February 2012.

[4] P. Mints, "Photovoltaic manufacturer shipments, capacity & competitive analysis 2010/2011," tech. rep., Navigant, April 2011.

[5] "U.s. solar market insight, report 2011 year-in-review, executive summary," tech. rep., US Energy Industries Association, GTM Research, 2012.

[6] "U.s. solar market insight, report q1 2012, executive summary," tech. rep., US Energy Industries Association, GTM Research, 2012.

[7] "Us solar industry year in review 2009," tech. rep., US Energy Industries Association, April 2010.

[8] S. C. John O. Blackburn, "Solar and nuclear costs - the historic crossover, solar energy is nor the better buy," tech. rep., Prepared for NC Warn, July 2010.

[9] "Best research-cell efficiencies," tech. rep., National Reneable Energy Labratory, 2012. http://www.nrel.gov/ncpv/images/efficiency_chart.jpg. Last accessed July 2012.

[10] R. Klenk and M. C. Lux-Steiner, *Chalcopyrite Based Solar Cells*, pp. 237–275. John Wiley & Sons, Ltd, 2006.

[11] M. A. Green, K. Emery, Y. Hishikawa, W. Warta, and E. D. Dunlop, "Solar cell efficiency tables (version 38)," *Progress in Photovoltaics: Research and Applications*, vol. 19, no. 5, pp. 565–572, 2011.

[12] A. M. Gabor, J. R. Tuttle, D. S. Albin, M. A. Contreras, R. Noufi, and A. M. Hermann, "High efficiency cuinxga1-xse2 solar cells made from (inx,ga1-x)2se3 precursor films," *Applied Physics Letters.*, vol. 65(2), pp. 198–200, 1994.

[13] J. Palm, V. Probst, A. Brummer, W. Stetter, R. Tlle, T. Niesen, S. Visbeck, O. Hernandez, M. Wendl, H. Vogt, H. Calwer, B. Freienstein, and F. Karg, "Cis module pilot processing applying concurrent rapid selenization and sulfurization of large area thin film precursors," *Thin Solid Films*, vol. 431432, pp. 514 – 522, 2003.

[14] M. E. Beck, A. Swartzlander-Guest, R. Matson, J. Keane, and R. Noufi, "Cuin(ga)se2-based devices via a novel absorber formation process," *Solar Energy Materials and Solar Cells*, vol. 64, no. 2, pp. 135 – 165, 2000.

[15] V. A. Akhavan, M. G. Panthani, B. W. Goodfellow, D. K. Reid, and B. A. Korgel, "Thickness-limited performance of cuinse2 nanocrystal photovoltaic devices," *Opt. Express*, vol. 18, pp. A411–A420, Sep 2010.

[16] Q. Guo, ed., *Selenization of copper indium gallium disulfide nanocrystal films for thin film solar cells*, 34th Photovoltaic Specialists Conference, IEEE, 2009.

[17] W. Liu, D. B. Mitzi, M. Yuan, A. J. Kellock, S. J. Chey, and O. Gunawan, "12% efficiency cuin(se,s)2 photovoltaic device prepared using a hydrazine solution process," *Chem. Mater.*, vol. 22, no. 3, p. 10101014, 2010.

[18] M. Harati, J. Jia, K. Giffard, K. Pellarin, C. Hewson, D. A. Love, W. M. Lau, and Z. Ding, "One-pot electrodeposition, characterization and photoactivity of stoichiometric copper indium gallium diselenide (cigs) thin films for solar cells," *Phys. Chem. Chem. Phys.*, vol. 12, pp. 15282–15290, 2010.

[19] J. Hollingsworth, K. Banger, M.-C. Jin, J. Harris, J. Cowen, E. Bohannan, J. Switzer, W. Buhro, and A. Hepp, "Single source precursors for fabrication of iiiivi2 thin-film solar cells via spray cvd," *Thin Solid Films*, vol. 431432, no. 0, pp. 63 – 67, 2003. Proceedings of Symposium B, Thin Film Chalcogenide Photovoltaic Materials, E-MRS Spring Meeting.

[20] D. B. Mitzi, M. Yuan, W. Liu, A. J. Kellock, S. J. Chey, V. Deline, and A. G. Schrott, "A high-efficiency solution-deposited thin-film photovoltaic device," *Advanced Materials*, vol. 20, no. 19, pp. 3657–3662, 2008.

[21] W. Wang, Y.-W. Su, and C. hung Chang, "Inkjet printed chalcopyrite cuinxga1xse2 thin film solar cells," *Solar Energy Materials and Solar Cells*, vol. 95, no. 9, pp. 2616 – 2620, 2011.

[22] B. D. Weil, S. T. Connor, and Y. Cui, "Cuins2 solar cells by air-stable ink rolling," *J. Am. Chem. Soc.*, vol. 132, no. 19, p. 66426643, 2010.

[23] M. Kaelin, D. Rudmann, F. Kurdesau, H. Zogg, T. Meyer, and A. Tiwari, "Low-cost cigs solar cells by paste coating and selenization," *Thin Solid Films*, vol. 480481, no. 0, pp. 486 – 490, 2005. EMRS 2004, Proceedings of Symposium O on Thin Film Chalcogenide Photovoltaic Materials, EMRS 2004 Conference, Strasbourg, France, May 24-28, 2004.

[24] U. Rau and M. Schmidt, "Electronic properties of zno/cds/cu(in,ga)se2 solar cells aspects of heterojunction formation," *Thin Solid Films*, vol. 387, no. 12, pp. 141 – 146, 2001. Proceeedings of Symposium N on Thin Film Photovoltaicmaterials of the E-MRS Spring Conference.

[25] A. Z. Su Huai Wei, "Band offsets at the cds/cuinse2 heterojunction," *Applied Physics Letters*, vol. 63, pp. 2549 – 2551, 1993.

[26] A. Klein and W. Jaegermann, "Fermi-level-dependent defect formation in cu-chalcopyrite semiconductors," *Applied Physics Letters*, vol. 74, no. 16, pp. 2283–2285, 1999.

[27] R. F. Pierret, *Semiconductor Device Fundamentals*. MA 01760-1500, USA: Addison Wesley Longman, 1996.

[28] J.-P. Colinge and C. A. Colinge, *Physics of Semiconductor Devices*. NY 10013, USA: Springer, 2006.

[29] B. G. Streetman and S. Banerjee, *Solid State Electrinic Devices*. New Jeresey 07458, USA: Prentice Hall, fifth ed., 2000.

[30] K. Ottosson, *The Role of i-AnO for Shunt Prevention in Cu(In,Ga)Se2-based Solar Cells*. PhD thesis, Uppsala Universitet, Sweden, 2006.

[31] J. Nelson, *The Physics of Solar Cells*. London WC2H 9HE: Impirial College Press, 2003.

[32] S. S. Hegedus and W. N. Shafarman, "Thin-film solar cells: device measurements and analysis," *Progress in Photovoltaics: Research and Applications*, vol. 12, no. 2-3, pp. 155–176, 2004.

[33] M. A. Green, *Solar cells: Operating principles, technology, and system applications*. 1982.

[34] E. van Dyk and E. Meyer, "Analysis of the effect of parasitic resistances on the performance of photovoltaic modules," *Renewable Energy*, vol. 29, no. 3, pp. 333 – 344, 2004.

[35] T. Dullweber, G. Hanna, W. Shams-Kolahi, A. Schwartzlander, M. Contreras, R. Noufi, and H. Schock, "Study of the effect of gallium grading in cu(in,ga)se2," *Thin Solid Films*, vol. 361362, no. 0, pp. 478 – 481, 2000.

[36] M. Gloeckler and J. Sites, "Band-gap grading in cu(in,ga)se2 solar cells," *Journal of Physics and Chemistry of Solids*, vol. 66, no. 11, pp. 1891 – 1894, 2005. The 14th International Conference on Ternary and Multinary Compounds.

[37] T. Meyer, F. Engelhardt, J. Parisi1, and U. Rau, "Spectral dependence and hall effect of persistent photoconductivity in polycrystalline cu(in,ga)se2 thin films," *Journal of Applied Physics*, vol. 91, pp. 5093–5099, 2002.

[38] J. Pohl and K. Albe, "Thermodynamics and kinetics of the copper vacancy in cuinse2, cugase2, cuins2, and cugas2 from screened-exchange hybrid density functional theory," *Journal of Applied Physics*, vol. 108, pp. 235–239, 2010.

[39] V. Chandrasekaran, *Effect of heat treatments and reduced absorber layer thickness on cu(in,ga)se2 thin film solar cells*. PhD thesis, University of South Florida, Sarasota, FL, 2005.

[40] S. Roschier, *Development of Procedures for Performance and Lifetime Testing of Thin Film Photovoltaic Devices*. PhD thesis, Helsinki University of Technology, Finland, 2002.

[41] A. Romeo, M. Terheggen, D. Abou-Ras, D. L. Btzner, F.-J. Haug, M. Klin, D. Rudmann, and A. N. Tiwari, "Development of thin-film cu(in,ga)se2 and cdte solar cells," *Progress in Photovoltaics: Research and Applications*, vol. 12, no. 2-3, pp. 93–111, 2004.

[42] T. Satoh, Y. Hashimoto, S. ichi Shimakawa, S. Hayashi, and T. Negami, "Cu(in,ga)se2 solar cells on stainless steel substrates covered with insulating layers," *Solar Energy Materials and Solar Cells*, vol. 75, no. 12, pp. 65 – 71, 2003.

[43] M. Pagliaro, R. Ciriminna, and G. Palmisano, "Flexible solar cells," *ChemSusChem*, vol. 1, no. 11, pp. 880–891, 2008.

[44] D. Bremaud, ed., *Towards the development of flexible CIGS solar cells on polymer films with efficiency exceeding 15%*, Photovoltaic Specialists Conference, IEEE, Jan 2005.

[45] K. Orgassa, H. Schock, and J. Werner, "Alternative back contact materials for thin film cu(in,ga)se2 solar cells," *Thin Solid Films*, vol. 431432, pp. 387 – 391, 2003. Proceedings of Symposium B, Thin Film Chalcogenide Photovoltaic Materials, E-MRS Spring Meeting.

[46] D. R. Friedrich Kesslera, "Technological aspects of flexible cigs solar cells and modules," *Solar Energy*, vol. 77, no. 6, pp. 685 – 695, 2004.

[47] I. Repins, M. A. Contreras, B. Egaas, C. DeHart, J. Scharf, C. L. Perkins, B. To, and R. Noufi, "19.9%-efficient zno/cds/cuingase2 solar cell with 81.2% fill factor," *Progress in Photovoltaics: Research and Applications*, vol. 16, no. 3, pp. 235–239, 2008.

[48] T. Wada, N. Koharab, S. Nishiwakib, and T. Negamib, "Characterization of the cu(in,ga)se2/mo interface in cigs solar cells," *Thin Solid Films*, vol. 387, no. 12, pp. 118 – 122, 2001. Proceeedings of Symposium N on Thin Film Photovoltaicmaterials of the E-MRS Spring Conference.

[49] L. Assmann, J. Bernde, A. Drici, C. Amory, E. Halgand, and M. Morsli, "Study of the mo thin films and mo/cigs interface properties," *Applied Surface Science*, vol. 246, no. 13, pp. 159 – 166, 2005.

[50] M. A. Green, K. Emery, Y. Hishikawa, and W. Warta, "Solar cell efficiency tables (version 36)," *Progress in Photovoltaics: Research and Applications*, vol. 18, no. 5, pp. 346–352, 2010.

[51] R. N. Bhattacharya, "High efficiency thin-film cuin1-xgaxse2 photovoltaic cells using a cd1-xznxs buffer layer," *Applied Physics Letters*, vol. 89, pp. 253503 – 253503–2, 2006.

[52] D. Hariskos, S. Spiering, and M. Powalla, "Buffer layers in cu(in,ga)se2 solar cells and modules," *Thin Solid Films*, vol. 480481, no. 0, pp. 99 – 109, 2005. EMRS 2004, Proceedings of Symposium O on Thin Film Chalcogenide Photovoltaic Materials, EMRS 2004 Conference, Strasbourg, France, May 24-28, 2004.

[53] A. Pudov, *Impact of Secondary Barriers on CuIn1-xGaxSe2 Solar-Cell Operation*. PhD thesis, Colorado State University, Colorado, 2005.

[54] M. Gloeckler and J. Sites, "Efficiency limitations for wide-band-gap chalcopyrite solar cells," *Thin Solid Films*, vol. 480481, no. 0, pp. 241 – 245, 2005. EMRS 2004, Proceedings of Symposium O on Thin Film Chalcogenide Photovoltaic Materials, EMRS 2004 Conference, Strasbourg, France, May 24-28, 2004.

[55] J. H. Scofield, A. Duda, D. Albin, B. Ballard, and P. Predecki, "Sputtered molybdenum bilayer back contact for copper indium diselenide-based polycrystalline thin-film solar cells," *Thin Solid Films*, vol. 260, no. 1, pp. 26 – 31, 1995.

[56] Q. Guo, S. J. Kim, M. Kar, W. N. Shafarman, R. W. Birkmire, E. A. Stach, R. Agrawal, and H. W. Hillhouse, "Devepolpment of cuinse2 nanocryatal and nanoring inks for low-cost solar cells," *Nano Letters*, vol. 8, no. 9, pp. 2982–2987, 2008.

[57] M. Kaelin, D. Rudmann, and A. Tiwari, "Low cost processing of cigs thin film solar cells," *Solar Energy*, vol. 77, no. 6, pp. 749 – 756, 2004. Thin Film PV.

[58] J. L. Gray, X. Wang, and X. Sun, "Adept 2.0," 2011.

[59] O. Lundberg, M. Bodegrd, J. Malmstrm, and L. Stolt, "Influence of the cu(in,ga)se2 thickness and ga grading on solar cell performance," *Progress in Photovoltaics: Research and Applications*, vol. 11, no. 2, pp. 77–88, 2003.

[60] D. Young, J. Abushama, R. Noufi, X. Li, J. Keane, T. Gessert, J. Ward, M. Contreras, M. Symko-Davies, and T. Coutts, "A new thin-film cugase2/cu(in,ga)se2 bifacial, tandem solar cell with both junctions formed simultaneously," *Photovoltaic Specialists Conference, 2002. Conference Record of the Twenty-Ninth IEEE*, pp. 608 – 611, May 2002.

[61] P. Bhattacharya, *Semiconductor Optoelectronic Devices*. USA: Prentice-Hall, second ed., 1997.

[62] C.-T. Sah, *Fundamentals of Solid State Electronics*. Singapore 9128: World Scientific, 1994.

APPENDICES

A. GENERATION AND RECOMBINATION

An electron needs to absorb energy at least equal to the band gap energy, Eg, to get excited and leave the valence band to conduction band. Likewise, if an electron in the conduction band combines with a hole in valance band, it will transfer its excess energy to a photon with energy of at least Eg. This process is called "band-to-band or direct" generation/recombination. If the electron and hole recombined(generated) by band-to-band process give off(absorb) their energy to(from) another electron or hole, the process is called "Auger" recombination(generation).

In ideal case, there are no permitted energy levels between the valence and conductance band. But in reality, semiconductors contain defects, making some energy levels, trap (Et), in the band gap. These defects could be excess, or missing, or dislocation of semiconductor atoms in the crystal or the existence of some impurities such as oxygen or metallic atoms in the structure. The energy level made by defects can receive or loose electron from valence or conductance band by absorbing less energy than Eg. Therefore, valance bands electron need to absorb energies less than Eg to travel to Et and then jump to conduction band. The same process happens for recombination, the conduction band electron radiates photons with energy less than Eg to move to Et and then transfer to valence band. This type of generation/recombination is called "Shockley-Read-Hall (SRH)". Recombination rate of electrons and holes are denoted by Rn and Rp. A trap that is neutral when it has an electron and positive when it is empty is called "donor level", and a level that is neutral when it is empty and negative when it is filled with an electron is called "acceptor level".

Recombination not only occurs in the bulk material, but also happens at the surface of the lattice. The surface of the semiconductor is where its lattice's periodicity gets interrupted, causing "surface recombination". The surface recombination rate is usually higher than the recombination in the bulk material. The surface recombina-

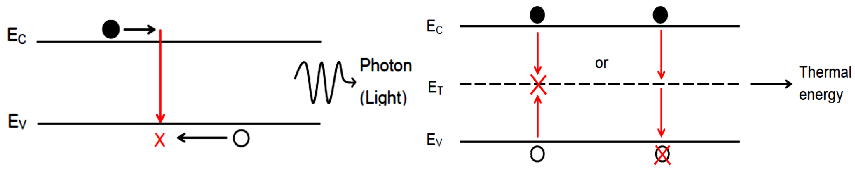

Fig. A.1 Band-to-Band(Direct) and Shockley-Read-Hall Recombinations

tion rate is denoted by Sp and Sn for holes and electrons and is defined as the number of electrons and holes disappearing at the surface of crystal per unit area per second.

A.1 Band-to-Band Recombination

In thermal equilibrium, the band-to-band(direct) recombination is proportional to the carrier concentrations and is found by

$$R^{DIR} = B^{DIR}.(np - n_i^2) \tag{A.1}$$

where B^{DIR} is band-to-band recombination coefficient with unit of $cm^3.s^{-1}$.

A.2 SRH Recombination

Let's consider an acceptor trap for SRH recombination. The recombination rate in such material would be proportional to the concentration of electrons in conduction band (n) and the concentration of neutral or empty traps. Therefore the SRH recombination rate for an electron on such trap would be

$$R_n^{SRH} = v_{th}\sigma_n n(N_t - n_t) = v_{th}\sigma_n n N_t(1 - \frac{n_t}{N_t}) = v_{th}\sigma_n n N_t(1 - f(E_t)) \tag{A.2}$$

where N_t is the density of traps, n_t is the concentration of electrons occupying the traps, v_th is the thermal velocity of electrons and σ_n is electron capture cross section. Electron capture cross section represents how close an electron must be to a trap

to be captured by it. Thermal velocity is the random motion of electron at a given temperature and could be found from:

$$\frac{1}{2}m_e v_{th}^2 = \frac{3}{2}kT \tag{A.3}$$

where m_e is effective mass of electron and $\frac{3}{2}kT$ is its thermal energy.

In Equation A.2, $f(E_t)$ is the Fermi-Dirac distribution at energy level of trap at thermodynamic equilibrium. Fermi-Dirac distribution of E_t is defined as the probability that energy level E_t is filled by an electron in thermal equilibrium.

$$f(E_t) = \frac{n_t}{N_t} = \frac{1}{1 + exp[\frac{E_t - E_F}{kT}]} \tag{A.4}$$

As shown in Equation A.2, R_n^{SRH} is proportional to the concentration of empty traps $(N_t - n_t)$. Likewise the SRH generation of electron is proportional to is proportional to n_t (concentration of traps filled by an electron).

$$G_n^{SRH} = e_n N_t f(E_t) \tag{A.5}$$

where e_n is the proportionality coefficient for hole and represents the probability of a hole emission by traps.

Similarly, the recombination rate for holes made by traps can be calculated from

$$R_p^{SRH} = v_{th}\sigma_p p N_t f(E_t) \tag{A.6}$$

The holes generation rate, where a hole can jump from a neutral trap to the valance band is proportional to the concentration of the traps with no electron $(N_t - n_t)$. Similar to Equation A.5,

$$G_p^{SRH} = e_p N_t (1 - f(E_t)) \tag{A.7}$$

where e_p is the proportionality coefficient for hole and represents the probability of a hole emission by trap.

Using Equation A.4 the number of filled traps can be found from

$$n_t = \frac{N_t}{1 + exp[\frac{E_t - E_F}{kT}]} \tag{A.8}$$

In thermodynamic equilibrium and in the absence of an internal potential the summation of recombination/generation rates for electrons or holes is zero.

$$U_n = R_n - G_n = 0 \tag{A.9a}$$

$$U_p = R_p - G_p = 0 \tag{A.9b}$$

Using Equations A.2, A.4 and A.9a

$$v_{th}\sigma_n n N_t(1 - f(E_t)) = e_n N_t f(E_t) \tag{A.10}$$

On the other hand, the concentration of electron carriers can be found from

$$n = n_i exp[\frac{E_F - E_i}{kT}] \tag{A.11}$$

where E_i is the intrinsic Fermi level and n_i is the intrinsic carrier concentration. Therefore, Equation A.10 can be rewritten as

$$v_{th}\sigma_n n_i exp[\frac{E_F - E_i}{kT}][N_t - \frac{N_t}{1 + exp[\frac{E_t - E_F}{kT}]}] = e_n \frac{N_t}{1 + exp[\frac{E_t - E_F}{kT}]} \tag{A.12}$$

which results in

$$e_n = v_{th}\sigma_n n_i exp[\frac{E_t - E_i}{kT}] \tag{A.13a}$$

Similarly, the hole proportionality coefficient could be found from

$$e_p = v_{th}\sigma_p n_i exp[\frac{E_i - E_t}{kT}] \tag{A.13b}$$

In steady state case, the recombination/generation rate of electrons and holes act as a pair. Therefore

$$\frac{\partial n_t}{\partial t} = U_n - U_p = 0 \tag{A.14}$$

which is equivalent to

$$U_n = R_n^{SRH} - G_n^{SRH} = U_p = R_p^{SRH} - G_p^{SRH} \tag{A.15}$$

using this equation and Equations A.2, A.5, A.6, and A.7 results in

$$v_{th}\sigma_n n N_t(1 - f(E_t)) - e_n N_t f(E_t) = v_{th}\sigma_p p N_t f(E_t) - e_p N_t(1 - f(E_t)) \tag{A.16}$$

Solving this equation for $f(E_t)$

$$f(E_t) = \frac{\sigma_n n + \sigma_p n_i exp[\frac{E_i - E_t}{kT}]}{\sigma_n(n + n_i exp[fracE_t - E_i kT]) + \sigma_p(p + n_i exp[\frac{E_i - E_t}{kT}])} \tag{A.17}$$

Therefore, the SRH generation/recombination rate could be calculated from

$$U = U_p = U_n = R_n^{SRH} - G_n^{SRH} = v_{th}\sigma_n n N_t(1 - f(E_t)) - e_n N_t f(E_t) \tag{A.18}$$

Implying Equations A.11, A.13 and A.17

$$U = \frac{v_{th}\sigma_n\sigma_p N_t(pn - n_i^2)}{\sigma_n(n + n_i exp[\frac{E_t - E_i}{kT}]) + \sigma_p(p + n_i exp[\frac{E_i - E_t}{kT}])} \tag{A.19a}$$

or in simpler form

$$U = \frac{pn - n_i^2}{\tau_n(n + n_i exp[\frac{E_t - E_i}{kT}]) + \tau_p(p + n_i exp[\frac{E_i - E_t}{kT}])} \tag{A.19b}$$

where tau_n and τ_p are the lifetime of electrons and holes in steady-states and are can be found by

$$\tau_n = \frac{1}{v_{th}\sigma_n N_t} \tag{A.20a}$$

$$\tau_p = \frac{1}{v_{th}\sigma_p N_t} \tag{A.20b}$$

The lifetime of minority and excess carriers are the same. It is clear from Equations A.19 that the recombination rate is maximum when the traps are located at the center of band gap.

A.3 Surface Recombination

The derivation of surface recombination is similar to the SRH in bulk material. The surface recombination van be found by a formula similar to Equations A.19

$$S = \frac{v_{th}\sigma_n\sigma_p N_{st}(p_s n_s - n_i^2)}{\sigma_n(n_s + n_i exp[\frac{E_{st} - E_i}{kT}]) + \sigma_p(p_s + n_i exp[\frac{E_i - E_{st}}{kT}])} \tag{A.21}$$

where N_st is the concentration of traps at the surface (cm^{-2}) and E_{st} is their energy. p_s and n_s are the hole and electron concentrations at the surface ($cm{-}3$). Similar to SRH in bulk material, the surface recombination rate is the highest when the surface traps are located at midgap. [27, 28, 61, 62]

B. SIMULATION PARAMETERS

This section presents parameters that were used in ADEPT 2.0 to for solar cell simulations. These general CIGS solar cell parameters were taken from literatures.

Table B.1 General Layer Properties Used in Base Case Simulation

	CIGS	**CdS**	**n-ZnO**
Thickness	1μm	50 nm	200 nm
Bandgap	1.15 ev	2.4 ev	3.3 ev
Dielectric Constant	13.6	10	9
NC Density of States	2.22×10^{18} cm^{-3}	2.22×10^{18} cm^{-3}	2.22×10^{18}cm^{-3}
NV Density of States	1.78×10^{19} cm^{-3}	2.22×10^{19} cm^{-3}	2.22×10^{19}cm^{-3}
Doping Density	2×10^{16}cm^{-3}	1×10^{17} cm^{-3}	2.22×10^{21}cm^{-3}
Electron Mobility	100 cm^2/Vs	100 cm^2/Vs	100 cm^2/Vs
Hole Mobility	25 cm^2/Vs	25 cm^2/Vs	25 cm^2/Vs
Electron Affinity	4.1 ev	3.8 ev	4.0 ev
SHR Electron Lifetime	$2 * 10^{-9}$s	$1 * 10^{-9}$ s	$1 * 10^{-12}$ s
SHR Hole Lifetime	$2 * 10^{-6}$s	$1 * 10^{-13}$ s	$1 * 10^{-9}$ s

Table B.2 Defect States Used in Base Case Simulation

	CIGS	**CdS**	**n-ZnO**
Defect Density of States	$1 \times 10^{14}\text{cm}^{-3}$	$1 \times 10^{18}\text{cm}^{-3}$	$1 \times 10^{17}\text{cm}^{-3}$
Standard Deviation	0.1	0.1	0.1
Donor's Trap Level	0.56 ev	1.2 ev	1.65 ev
Acceptor's Trap Level	0.56 ev	1.2 ev	1.65 ev
Electron Capture Cross Section	1×10^{-15} cm^2	1×10^{-12} cm^2	$1 \times 10^{-15}\text{cm}^2$
Hole Capture Cross Section	1×10^{-13} cm^2	1×10^{-17} cm^2	$1 \times 10^{-12}\text{cm}^2$

Table B.3 General Device Properties Used in Base Case Simulation

	Back Contact	**Front Contact**
Electron Surface Recombination Velocity	10^7 cm/s	10^7 cm/s
Hole Surface Recombination Velocity	10^7 cm/s	10^7 cm/s